

1-1-2009

Improving Power Density Of A Class Of Piezoelectric Power Harvesters Through Proof Mass Optimization

Wen G. Li
Ryerson University

Follow this and additional works at: <http://digitalcommons.ryerson.ca/dissertations>



Part of the [Mechanical Engineering Commons](#)

Recommended Citation

Li, Wen G., "Improving Power Density Of A Class Of Piezoelectric Power Harvesters Through Proof Mass Optimization" (2009).
Theses and dissertations. Paper 1150.

This Thesis is brought to you for free and open access by Digital Commons @ Ryerson. It has been accepted for inclusion in Theses and dissertations by an authorized administrator of Digital Commons @ Ryerson. For more information, please contact bcameron@ryerson.ca.

TK
7872
.P54
L5
2009

IMPROVING POWER DENSITY OF A CLASS OF
PIEZOELECTRIC POWER HARVESTERS
THROUGH PROOF MASS OPTIMIZATION

by

Wen Guang Li

B.Eng., Ryerson University, 2007

A thesis

presented to Ryerson University

in partial fulfillment of the

requirement for the degree of

Master of Applied Science

in the Program of

Mechanical Engineering

Toronto, Ontario, Canada, 2009

© Wen Guang Li 2009

PROPERTY OF
RYERSON UNIVERSITY LIBRARY

I hereby declare that I am the sole author of this thesis.

I authorize Ryerson University to lend this thesis or dissertation to other institutions or individuals for the purpose of scholarly research.

Wen Guang Li

Date

I further authorize Ryerson University to reproduce this thesis or dissertation by photocopying or by other means, in total or in part, at the request of other institutions or individuals for the purpose of scholarly research.

Abstract

IMPROVING POWER DENSITY OF A CLASS OF PIEZOELECTRIC POWER HARVESTERS THROUGH PROOF MASS OPTIMIZATION

by

Wen Guang Li

Master of Applied Science in Mechanical Engineering
Ryerson University, Toronto, 2009.

This thesis presents a method to optimize the proof mass of the cantilever piezoelectric power harvester. With this novel proof mass, a lower fundamental frequency and a higher power density (output power per unit volume) were achieved. Prototypes of 0.242 cm^3 in volume were fabricated and tested and a power density of $1446 \text{ } \mu\text{W}/\text{cm}^3$ was achieved for sinusoidal excitation of 0.75 g. It was experimentally shown that the new power harvester lowered the fundamental frequency by 26% and increased the power density by 68% in comparison with the conventional harvesters. When tested on a shoe, the new power harvester generated an average power of $48.4 \text{ } \mu\text{W}$ at 3.0 mph walking speed on a treadmill.

Acknowledgement

Throughout the course of my graduate studies, I have had the opportunity to work with a wide range of people. I wish to take this time to acknowledge those who have helped and inspired me.

I would like to thank Prof. Siyuan He for giving me the opportunity to work in the field of power harvesting and pushing me to achieve my goals. I am very grateful for his support and guidance throughout the course of this project.

I would like to thank Prof. Shudong Yu for acting as co-advisor of this project. I am very grateful for his support, technical advice and guidance throughout the project.

I would like to thank Chao Ma, Joseph Amankrah, and Devin Ostrom for their technical advice and support.

I am extremely thankful to Peter Bulski for his friendship and athleticism, without whom, the countless hours of treadmill tests would not have been possible.

My lab mates, John Chang and Anthony Chiu, have made my graduate studies a very enjoyable one. I am grateful for their moral support and friendship.

Finally, I would like to thank my family for their love and support.

Table of Contents

Abstract	iii
Acknowledgement.....	iv
Table of Contents	v
List of Tables.....	vi
List of Figures	vii
Chapter 1: Introduction	1
1.1 Low Power Electronic Devices	1
1.2 Problems With Battery Powered Electronic Devices.....	2
1.3 Power Harvesting From Mechanical Vibrations.....	2
1.4 Conventional Piezoelectric Power Harvesters	5
1.5 Proposed Solution to Improving the Cantilever Power Harvester	6
Chapter 2: Optimal Shape of Proof Mass.....	8
2.1 Curved L-Shape Mass	8
2.2 Design of Curved L-Shape Mass Harvester.....	10
2.2.1 Design Constraints	10
2.2.2 ANSYS Model	14
2.2.3 Procedure For Designing the Curved L-shape Mass Harvester.....	15
Chapter 3: Comparison of Simulation Results of Curved L-Shape Mass Harvester With Conventional Mass Harvesters.....	21
3.1 Fixed Fundamental Frequency	21
3.1.1 Block Shape Mass Harvester	21
3.1.2 U-Shape Mass Harvester.....	23
3.1.3 Comparison of Different Proof Mass Harvesters With Fixed Fundamental Frequency	24
3.2 Fixed Overall Volume.....	26

3.2.1 Block Shape Mass Harvester	26
3.2.2 U-Shape Mass Harvester.....	27
3.2.3 Comparison of Different Mass Harvesters With Fixed Overall Volume	27
Chapter 4: Fabrication and Assembly of Prototypes.....	29
Chapter 5: Experimental Testing on a Shaker.....	38
5.1 Setup of the Shaker Experiment.....	38
5.2 Shaker Test Results of Curved L-Shape Power Harvester 1, 2 and 3	39
5.2.1 Fundamental Frequency of Curved L-Shape Mass Harvester	39
5.2.2 Power Output of Curved L-Shape Mass Harvester.....	41
5.3 Shaker Results of the Block Shape Power Harvester.....	47
5.3.1 Fundamental Frequency of Block Shape Mass Harvester	47
5.3.2 Power Output of Block Shape Mass Harvester.....	49
5.4 Comparison of Block Shape and Curved L-Shape Power Harvester's Shaker Results.....	52
Chapter 6: Power Harvesting from Human Body's Motion	54
Chapter 7: Conclusions and Recommendations for Future Work.....	60
Publications	62
References	63

List of Tables

Table 2.1 Properties of the piezoelectric beam and tungsten mass	10
Table 2.2 Design parameters of the beam and proof mass.....	12
Table 2.3 Results of intermediate steps to the final curved L-shape mass design	18
Table 3.1 Results of intermediate steps to a 65 Hz block shape mass harvester.	22
Table 3.2 Results of intermediate steps to a 65 Hz U-shape mass harvester.	24

Table 3.3 Simulation results of different proof mass power harvester with 65 Hz fundamental frequency.....	26
Table 3.4 Simulation results of different proof mass power harvester with 0.242 cm ³ fixed overall volume.....	28

List of Figures

Figure 1.1 Photographs of various low power consumption devices: (a) a pressure sensor [2], (b) an acceleration sensor [2], (c) a highly integrated single-chip wireless network node [3], and (d) an artificial pacemaker [4].....	1
Figure 1.2 Schematic of an electromagnetic power harvester [7].....	3
Figure 1.3 Schematic of an electrostatic power harvester [11].....	4
Figure 1.4 Schematic of a piezoelectric power harvester.....	4
Figure 1.5 (a) Schematic of a conventional piezoelectric power harvester with a block mass and (b) volume of the block mass power harvester.....	6
Figure 2.1 (a) Schematic of a piezoelectric power harvester with a curved L-shape mass, and (b) curved L-shape mass profile that follows the mode shape of the beam.	9
Figure 2.2 Overall volume of curved L-shape mass harvester compared with block shape mass harvester.	9
Figure 2.3 (a) Schematic of a flat L-shape mass in the undeformed state and (b) wasted space of the flat L-shape mass in the deformed state. (c) utilizing the wasted space with a curved mass that follows the mode shape of the beam and (d) schematic of a piezoelectric power harvester with curved L-shape mass.	11
Figure 2.4 Cross-section of the piezoelectric composite beam.....	14
Figure 2.5 ANSYS model of curved L-shape mass harvester with base not shown.....	14
Figure 2.6 ANSYS model of curved L-shape mass harvester with mesh.....	15
Figure 2.7 ANSYS model of a flat L-shape mass, (a) undeformed state and (b) node numbers in each element of the mesh and (c) deformed state showing the mode shape of the beam.	16
Figure 2.8 The beam and mass nodes used in the data processing of the simulation results.	16

Figure 2.9 ANSYS model of the curved L-shape mass, (a) undeformed state and (b) deformed state showing the mode shape of the beam.....	18
Figure 2.10 Change of mass profile from final flat L-shape to final curved L-shape.....	18
Figure 2.11 Graphical illustration of the finalized curved L-shape mass.	19
Figure 2.12 Flow chart for design of curved L-shape mass harvester.	20
Figure 3.1 Schematic of a piezoelectric power harvester with a block shape mass.....	22
Figure 3.2 ANSYS model of the block shape mass harvester, (a) undeformed state and (b) deformed state showing the mode shape of the beam.....	22
Figure 3.3 Schematic of a piezoelectric power harvester with a U-shape mass.	24
Figure 3.4 ANSYS model of the U-shape mass harvester, (a) undeformed state and (b) deformed state showing the mode shape of the beam.....	24
Figure 3.5 Maximum allowed tip displacement of: (a) curved L-shape mass harvester, (b) block shape mass harvester and (c) U-shape mass harvester.	25
Figure 4.1 Piezoelectric power harvester prototype with, (a) Tungsten block shape mass and (b) Tungsten curved L-shape mass.....	29
Figure 4.2 Components of the piezoelectric power harvester prototype.....	30
Figure 4.3 Wire EDM profile of the Tungsten proof mass in the raw material.....	31
Figure 4.4 Graphical illustration of (a) curved L-shape mass profile and (b) block shape mass profile. All dimensions are in millimeters.....	31
Figure 4.5 Piezoelectric composite beam (T215-H4-103Y).	32
Figure 4.6 Schematic of the PZT composite beam cross-section.	32
Figure 4.7 Connections of the piezoelectric beam in (a) series and (b) parallel.	32
Figure 4.8 (a) Exposed shim area of the piezoelectric beam and (b) Grinding bit used to expose the shim.	33
Figure 4.9 CAD drawing of the base (dimensions are in millimeters).	34
Figure 4.10 CAD drawing of the casing (dimensions are in millimeters).	35
Figure 4.11: Attachment of the beam to the base.....	35
Figure 4.12 Clamping the piezoelectric beam to (a) plastic base and (b) mass.	36

Figure 4.13 Soldered connections of the power harvester.	36
Figure 4.14 Completed curved L-shape mass piezoelectric power harvester.	37
Figure 4.15 Limiting the tip displacement of using the casing and stoppers.	37
Figure 5.1 Setup of the power harvester on the shaker.	38
Figure 5.2 Complete setup of the shaker experiment.	39
Figure 5.3 Block diagram of the setup of the shaker experiment.	39
Figure 5.4 Open-circuit voltage output of curved L-shape harvester 1 at 60 Hz @ 0.75 g.	40
Figure 5.5 Peak open-circuit voltage versus frequency of curved L-shape harvester 1, 2 and 3 at different input accelerations.	41
Figure 5.6 Voltage measurement of curved L-shape 1 at 60.5 Hz @ 0.75 g for a resistive load of 80 k Ω	42
Figure 5.7 Voltage versus frequency at different resistive loads for a fixed input acceleration of 0.75 g. (a) curved L-shape harvester 1, (b) curved L-shape harvester 2 and (c) curved L-shape harvester 3.	44
Figure 5.8 Power versus frequency of different resistive loads for a fixed input acceleration of 0.75 g. (a) curved L-shape harvester 1, (b) curved L-shape harvester 2 and (c) curved L-shape harvester 3.	45
Figure 5.9 Voltage versus resistive loads for curved L-shape harvesters 1, 2, and 3 at an input acceleration of 0.75 g.	47
Figure 5.10 Power versus resistive loads for curved L-shape harvesters 1, 2, and 3 at an input acceleration of 0.75 g.	47
Figure 5.11 Open-circuit voltage output of block shape harvester at 87 Hz @ 0.75 g.	48
Figure 5.12 Peak open-circuit voltage versus frequency of block shape harvester at different input accelerations.	49
Figure 5.13 Voltage measurement of block shape harvester at 86.5 Hz @ 0.75 g for a resistive load of 40 k Ω	49
Figure 5.14 Voltage versus frequency of block shape harvester at different resistive loads for a fixed input of 0.75 g.	50
Figure 5.15 Power versus frequency of block shape harvester at different resistive loads for a fixed input of 0.75 g.	51

Figure 5.16 Voltage versus resistive loads for block shape harvester at a fixed input of 86.5Hz @ 0.75 g.	52
Figure 5.17 Power versus resistive loads for block shape harvester at a fixed input of 86.5Hz @ 0.75 g.	52
Figure 6.1 Setup of the walking experiment.	54
Figure 6.2 Attachment of the power harvester on the shoe.....	55
Figure 6.3 Block diagram of the treadmill experiment setup.....	55
Figure 6.4 Measured acceleration versus time at different walking speeds.....	56
Figure 6.5 Output voltage of curved L-shape harvester versus time at different walking speeds.	57
Figure 6.6 Open-circuit RMS voltage versus walking speed.....	58
Figure 6.7 RMS voltage versus resistive load at different walking speeds.....	59
Figure 6.8 Power output versus resistive load at different walking speeds.	59

Chapter 1: Introduction

1.1 Low Power Electronic Devices

Advances in integrated circuit (IC) manufacturing, low power IC circuits and MEMS technology have enabled many electronic devices to be more energy efficient. These low power devices include wireless sensors, implanted medical devices and hand-held electronic devices. They consume tens to hundreds of microwatts of power [1]. A few examples of low power electronic devices are pressure sensors, acceleration sensors, wireless sensor network nodes and artificial pacemakers. A MEMS pressure sensor (SMD500) by Bosch Sensortec is shown in Figure 1.1a. The $5\text{ mm} \times 5\text{ mm} \times 1.5\text{ mm}$ pressure sensor consumes $18\text{ }\mu\text{W}$ of power. Another MEMS sensor by Bosch Sensortec, shown in Figure 1.1b, is the triaxial acceleration sensor (SMB380). The $3\text{ mm} \times 3\text{ mm} \times 0.9\text{ mm}$ acceleration sensor consumes $720\text{ }\mu\text{W}$ of power in operation mode and $3.6\text{ }\mu\text{W}$ in idle mode [2].

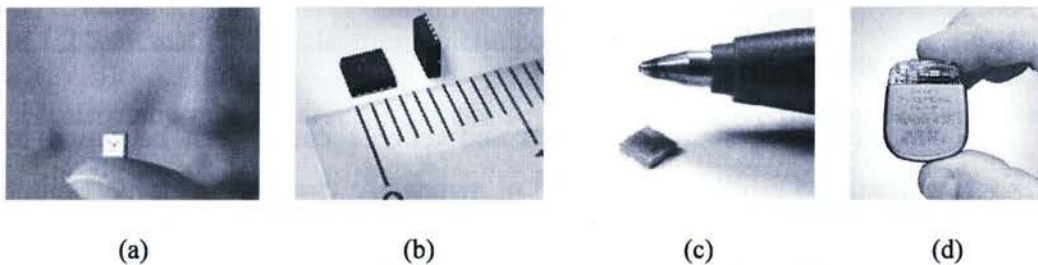


Figure 1.1 Photographs of various low power consumption devices: (a) a pressure sensor [2], (b) an acceleration sensor [2], (c) a highly integrated single-chip wireless network node [3], and (d) an artificial pacemaker [4].

A highly integrated single-chip wireless network node (Spec) by JLH Labs is shown in Figure 1.1c. A CPU, memory, an analog to digital converter for reading sensor data and an ultra-low power radio transmitter are all integrated onto a single $2.5\text{ mm} \times 2.5\text{ mm}$ piece of silicon [3]. Each wireless network node consumes less than $10\text{ }\mu\text{W}$ of

power in idle mode and when combined with a sensor, the entire system can last several years with a single battery charge.

An implanted medical device is the artificial pacemaker (Microny K 2535K) shown in Figure 1.1d. The size of the pacemaker is 5.9 cm^3 and weights 12.8 g, its life with a single battery charge is approximately 5-8 years [4].

1.2 Problems With Battery Powered Electronic Devices

The predominant power sources for low power electronic devices are disposable and rechargeable batteries. Disposable batteries (e.g., alkaline) are discarded after being used once and rechargeable batteries (e.g., lithium ion) can be recharged and re-used for many times. The main drawbacks of battery powered systems include: 1) limited energy supply, which limits the duration of operation; 2) frequent battery maintenance and replacement, which are inconvenient or impossible for some applications such as implanted medical devices and remote monitoring/tracking devices; and 3) adverse environmental effects. Millions of batteries are thrown away each year, which are non-recyclable and non-biodegradable [5].

An alternative source of green and reliable energy can be found in low-level vibrations, which occur in many different environments (e.g., bridges, buildings, machinery, human body, etc.). This vibration energy can be harvested for low power electronic devices such that batteries can be eliminated or the life of batteries can be extended.

1.3 Power Harvesting From Mechanical Vibrations

There are three typical methods to harvest electrical power from mechanical vibrations. They are electromagnetic [6-9], electrostatic [10-12], and piezoelectric [13,

14] power harvesting. Electromagnetic power harvesting is the result of the relative motion of an electrical conductor coil in a magnetic field. The relative motion between the coil and the magnetic field causes a current to flow in the coil (see Figure 1.2). The main advantage of electromagnetic power harvester is that no additional electrical power source required. However, an electromagnetic harvester of 1 cm^3 can only produce voltage of 0.1 V and typical electronics require 2 V to 5 V to operate. Also, electromagnetic power harvesters cannot be easily integrated with electronics and microsystems [15].

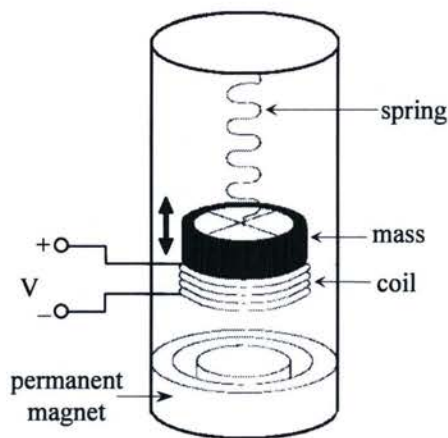


Figure 1.2 Schematic of an electromagnetic power harvester [7].

Electrostatic power harvesting is the result of the relative motion between charged electrodes (variable capacitor). As shown in Figure 1.3, charges are applied to the fixed and moving electrodes of the harvester. As distance between the charged electrodes varies, the capacitance between the electrodes varies [11]. When the capacitance increases, the voltage can be increased with a constant charge. When the capacitance decreases, the charges can be increased with a constant voltage. In either case, the energy in the variable capacitor increases [15]. The advantages of electrostatic power harvesters are: 1) easy integration with electronics and Microsystems, and 2) produces useful voltage levels from 2 to 10 volts. A major drawback of electrostatic power harvesters is

that an additional power source is required to supply the initial charges [15].

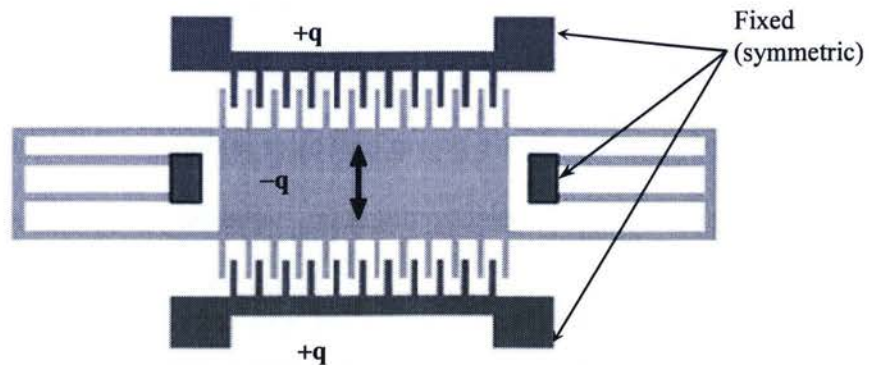


Figure 1.3 Schematic of an electrostatic power harvester [11].

Piezoelectric power harvesting utilizes the piezoelectric effect of smart materials, such as Lead Ziconate Titanate (PZT), to convert mechanical vibrations into electrical power. When such a piezoelectric material is strained, electrical charges are produced (see Figure 1.4). The major advantages of piezoelectric power harvesters are: 1) no additional electrical power source required, 2) production of useful voltage levels from 2 to 10 volts, and 3) the highest power density (power per unit volume) among the three power harvesting methods [15].

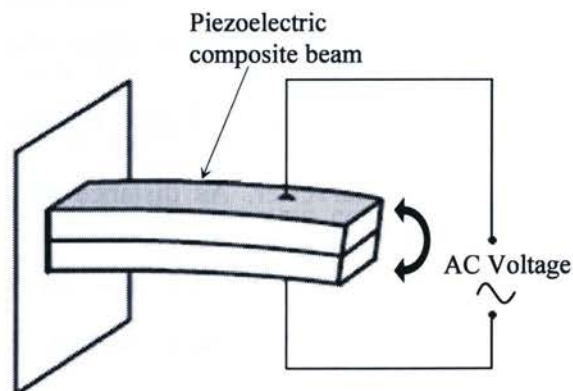


Figure 1.4 Schematic of a piezoelectric power harvester.

In summary, piezoelectric power harvesting offers the advantages of both electrostatic and electromagnetic power harvesting, i.e., produces a useful voltage from 2

to 10 V, and requires no additional power source. In addition, the high power density allows piezoelectric power harvesters to produce same amount of power with a smaller size, typically $\sim 1 \text{ cm}^3$ in volume. Piezoelectric power harvesting is studied in this thesis.

1.4 Conventional Piezoelectric Power Harvesters

There are many different piezoelectric power harvester designs in the literature, e.g., cantilever beam design [14-28], piezoelectric windmill design [29-34], and piezoelectric stack design [35-43]. Comprehensive reviews of the latest technologies in piezoelectric power harvesting can be found in [44-47].

The most popular piezoelectric power harvester design is the cantilever beam design. A block mass is usually attached at the free end to increase the strain in the beam (see Figure 1.5a). The advantages of the cantilever harvester design include low stiffness and high strain for a given size and input vibrations [15]. Hence, it is suitable for scavenging power from low frequency and low amplitude ambient vibrations, which ranges from 1 Hz of heart beating frequency to 120 Hz of rotating machinery frequency. When the power harvester's natural frequency (usually the fundamental frequency for cantilever beam harvester) matches the input frequency, it generates the highest power [16]. The power density of a power harvester is often used as an indicator for its performance.

The piezoelectric power harvester requires a protective casing to prevent it from bending beyond the maximum allowed displacement during operation and handling. The overall volume of the power harvester is the box volume (dashed line shown in Figure 1.5b) that encloses the piezoelectric beam and the proof mass [15].

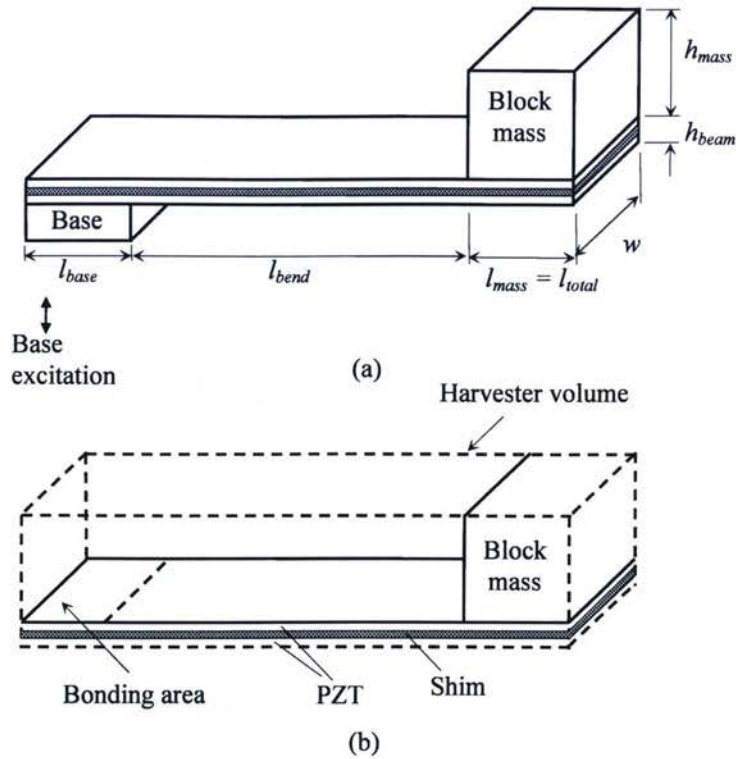


Figure 1.5 (a) Schematic of a conventional piezoelectric power harvester with a block mass and (b) volume of the block mass power harvester.

1.5 Proposed Solution to Improving the Cantilever Power Harvester

To increase the power density of the cantilever power harvester, a great deal of research has focused on:

- 1) Utilization of different piezoelectric materials
 - polymer piezoelectric beams and Polyvinylidene Fluoride (PVDF) were used to reduce the fundamental frequency and achieve higher strains in beam to increase generated power [17-19].
 - piezofiber composite beams were used to increase the generated power [19-22].
- 2) Utilization of different piezoelectric beam geometry
 - triangular and trapezoidal beam shapes were used to increase the

generated power [23-25].

3) Optimization of power harvesting circuit

- Using techniques such as synchronous switch harvesting on inductor and step-down DC-DC converter to increase power transfer compared to standard circuits [48-56].

In this thesis, the proof mass of the conventional cantilever harvester is optimized. As shown in Figure 1.5b, the volume of conventional cantilever harvester is not fully utilized by the block shape mass and a lot of space above the beam is wasted. This thesis presents a new proof mass that utilizes the wasted space to increase the mass of the system without increasing the overall volume. This new proof mass results in a lower fundamental frequency and higher power density.

Chapter 2: Optimal Shape of Proof Mass¹

The optimal proof mass for the cantilever piezoelectric power harvester is presented in this chapter. A detailed design procedure of the proof mass is demonstrated using an example piezoelectric power harvester and iterations in FEM simulations are used to complete the new design.

2.1 Curved L-Shape Mass

A curved L-shape proof mass, shown in Figure 2.1a, is proposed for the piezoelectric power harvester. The mass extends from the beam tip back to the base with its curved bottom surface following the fundamental mode shape of the beam (see Figure 2.1b). Thus, the curved L-shape mass design utilizes the space above the beam, wasted space of block mass design, to introduce more mass without increasing the overall volume (see Figure 2.2). Since more mass induces more strain on the piezoelectric beam, more power is generated for the same input excitation. Therefore, the curved L-shape mass harvester achieves a higher power density than the conventional block mass harvester [15]. In addition, the curved L-shape design results in a lower fundamental frequency because it accommodates more mass for a given volume. A lower fundamental frequency is preferred for many practical applications with low frequency ambient vibrations (e.g., human body movement, building vibration, wind-induced vibration, etc.) because the power harvester generates the highest power when its natural frequency matches the input frequency [15].

¹ A paper “Improving Power Density of a Cantilever Piezoelectric Power Harvester Through a Curved L-shape Proof Mass” based on the contents of Chapter 2, 3, 5, and 6 has been accepted for publication in IEEE Transaction on Industrial Electronics.

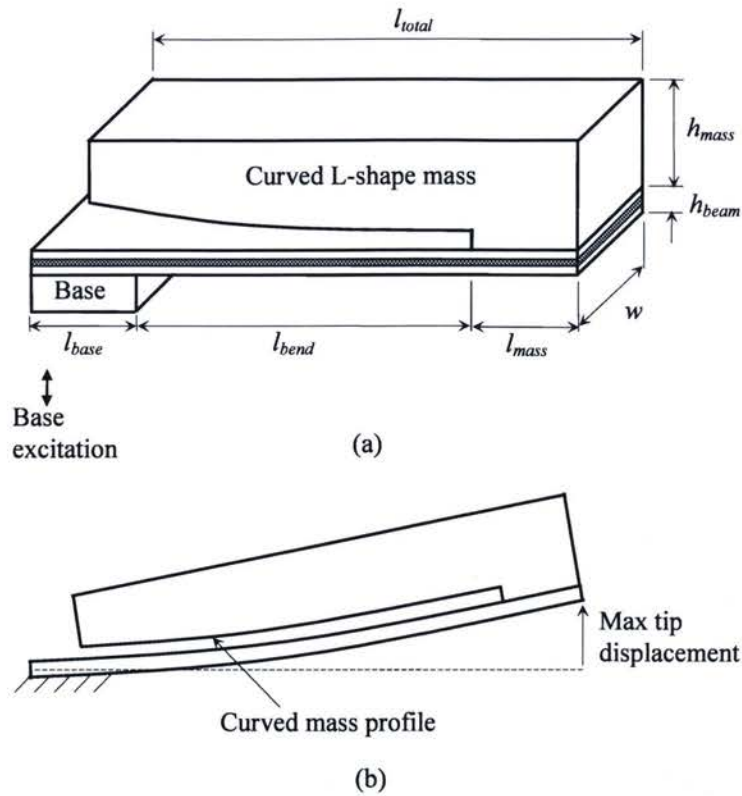


Figure 2.1 (a) Schematic of a piezoelectric power harvester with a curved L-shape mass, and (b) curved L-shape mass profile that follows the mode shape of the beam.

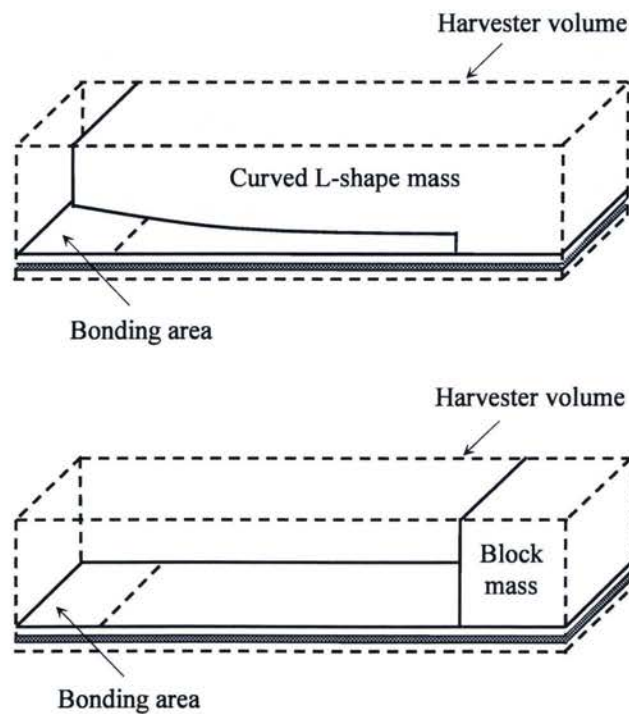


Figure 2.2 Overall volume of curved L-shape mass harvester compared with block shape mass harvester.

2.2 Design of Curved L-Shape Mass Harvester

2.2.1 Design Constraints

An example piezoelectric power harvester is used to demonstrate the design procedure of the curved L-shape mass harvester. The example harvester consists of a bimorph beam (two layers of piezoelectric material) and a Tungsten alloy proof mass. Their properties are given in Table 2.1. The design was constrained to a fundamental frequency (f) of 65 Hz, a safety margin (d_{safe}) of 0.2 mm when the tip displacement reaches a maximum value 1 mm (see Figure 2.3c). The safety margin was used to prevent the mass from contacting the beam and accommodate for any fabrication and assembly errors.

Table 2.1 Properties of the piezoelectric beam and tungsten mass

Quantity	PZT	Brass Shim	Tungsten Mass
Young's modulus (10^9 Pa)	62	100	450
Poisson's ratio	0.34	0.34	0.28
Density (kg/m^3)	7800	8400	17500
Strain Coefficient (10^{-12} m/V)	320	-	-
Dielectric constant (ϵ/ϵ_0)	3800	-	-
Length (mm)	32	32	-
Width (mm)	3.2	3.2	3.2
Thickness (mm)	0.139	0.102	-

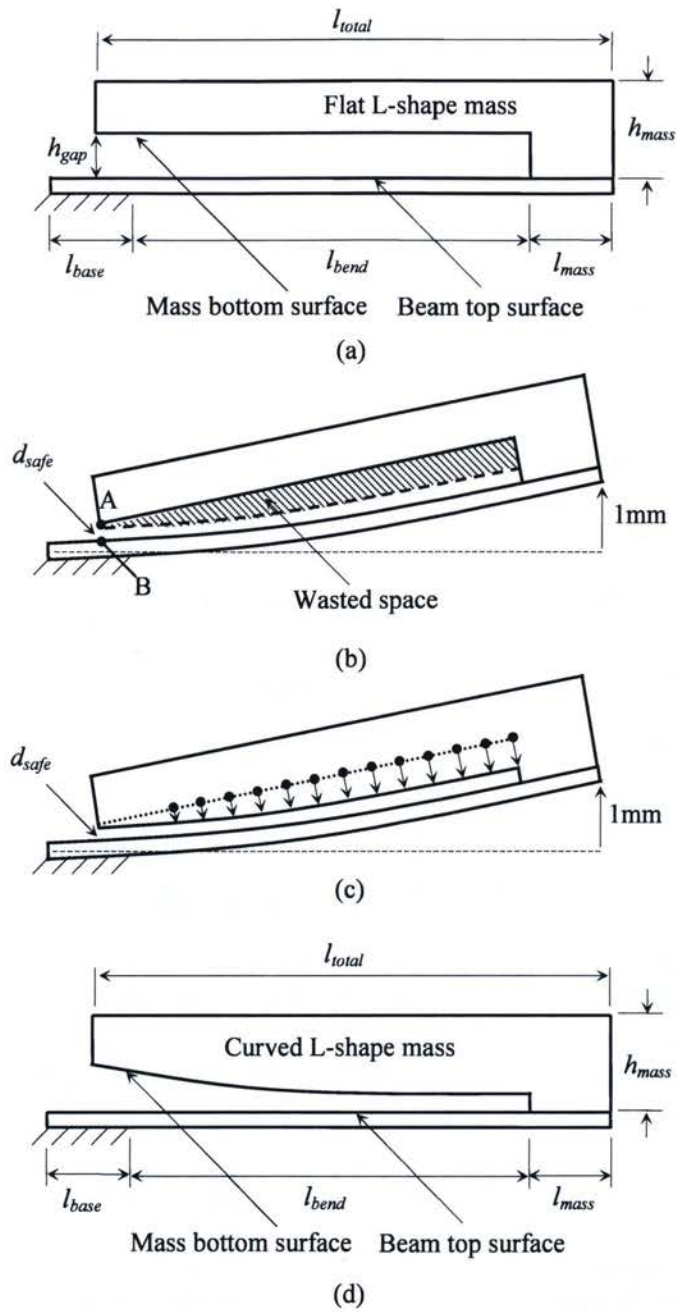


Figure 2.3 (a) Schematic of a flat L-shape mass in the undeformed state and (b) wasted space of the flat L-shape mass in the deformed state. (c) utilizing the wasted space with a curved mass that follows the mode shape of the beam and (d) schematic of a piezoelectric power harvester with curved L-shape mass.

The total length of the beam was 32 mm; 5 mm was reserved for bonding the base (l_{base}) and 5 mm for bonding the mass (l_{mass}). Thus, the free bending length (l_{bend}) was 22 mm (see Figure 2.3d). Since the beam was bonded to the base at the bottom surface, the mass can go beyond the bonding part and a 30 mm total mass length (l_{total}) was used. The widths (w) of the mass and beam were 3.2 mm. The mass height (h_{mass}) was used to tune the fundamental frequency of the harvester to 65 Hz and the gap height (h_{gap}) was used to tune the safety margin (d_{safe}) to 0.2 mm (see Figure 2.3d). The design parameters are summarized in Table 2.2.

Table 2.2 Design parameters of the beam and proof mass

Quantity	Beam	Proof Mass
l_{base} (mm)	5	-
l_{bend} (mm)	22	-
l_{mass} (mm)	5	5
l_{total} (mm)	-	30
h_{mass} (mm)	-	Design variable
h_{gap} (mm)	-	Design variable

Equations (2.1) [57], equation (2.2) [57], equation (2.3) [14] and equation 2.4 were used to estimate an initial h_{mass} for the ANSYS simulations [58].

$$f = \frac{1}{2\pi} \sqrt{\frac{k}{m}} \quad (2.1)$$

Where f is the fundamental frequency of the system, k is the stiffness of the beam and m is the proof mass (assumed to be a point mass).

$$k = \frac{3E_{eq} \cdot I}{l_{bend}^3} \quad (2.2)$$

Where E_{eq} is the equivalent Young's modulus of the composite beam; I is the moment of inertia of beam cross-sectional area; and l_{bend} is the free bending length of the beam.

$$E_{eq}I = E_{sh} \cdot \frac{w \cdot t_{sh}^3}{12} + 2E_{pzt} \left(\frac{w \cdot t_{pzt}^3}{12} + w \cdot t_{pzt} \cdot d^2 \right) \quad (2.3)$$

Where E_{sh} is the Young's modulus of the shim; E_{pzt} is the Young's modulus of the PZT; w is the width of the beam, t_{sh} is the thickness of the shim layer; t_{pzt} is the thickness of the PZT layer; and d is the distance between the center of the PZT layer to the center of the shim layer (see Figure 2.4).

$$\forall = w \left[l_{total} \cdot h_{mass} - h_{gap} (l_{total} - l_{mass}) \right] = \frac{m}{\rho} \quad (2.4)$$

Where \forall is the volume of the proof mass; ρ is the density of the proof mass; l_{total} is the maximum length of the mass; l_{mass} is the length of the interface between the mass and the beam; h_{mass} is the height of the mass; and h_{gap} is the height of the gap between the mass and the beam (see Figure 2.3a).

The proof mass was calculated by substituting equation (2.2) and (2.3) into equation (2.1). Then an initial value was chosen for h_{gap} (e.g., 1 mm) and h_{mass} was calculated by using equation (2.4). Using the estimated initial h_{mass} , simulations in ANSYS were performed to fine tune the h_{mass} and h_{gap} to achieve a fundamental frequency of 65 Hz with a safety margin of 0.2 mm.

Iterations in ANSYS simulations were required to determine the final values of h_{mass} and h_{gap} and equations (2.5) – (2.7) were used to estimate values of h_{mass} and h_{gap} for the next simulation trial. Equations (2.5) – (2.7) were developed based on trial and error of many rounds of simulation.

$$h_{mass_i} = h_{mass_{i-1}} + \left(f_{i-1} - 65\text{Hz} \right) \cdot \left| \frac{h_{mass_{i-1}} - h_{mass_{i-2}}}{f_{i-1} - f_{i-2}} \right| \quad (2.5)$$

$$h_{gap_i} = h_{gap_{i-1}} - (d_{safe_{i-1}} - 0.2mm) \quad (2.6)$$

$$h_{mass_i} = h_{mass_{i-1}} + (f_{i-1} - 65Hz) \cdot \left| \frac{h_{gap_{i-1}} - h_{gap_{i-2}}}{f_{i-1} - f_{i-2}} \right| \quad (2.7)$$

2.2.2 ANSYS Model

The bimorph PZT piezoelectric beam, which consists of two PZT layers sandwiched onto a brass shim layer (see Figure 2.4), and tungsten alloy proof mass were modeled in ANSYS (see Figure 2.5). The properties of the composite beam and proof mass are given in Table 2.1.

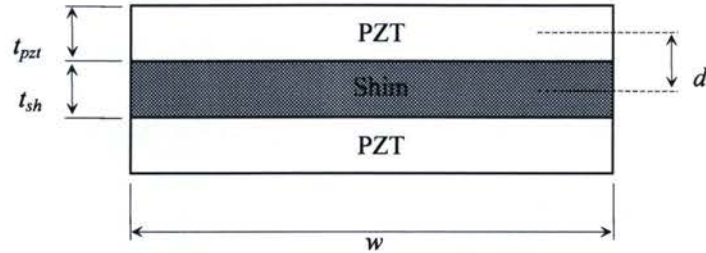


Figure 2.4 Cross-section of the piezoelectric composite beam.

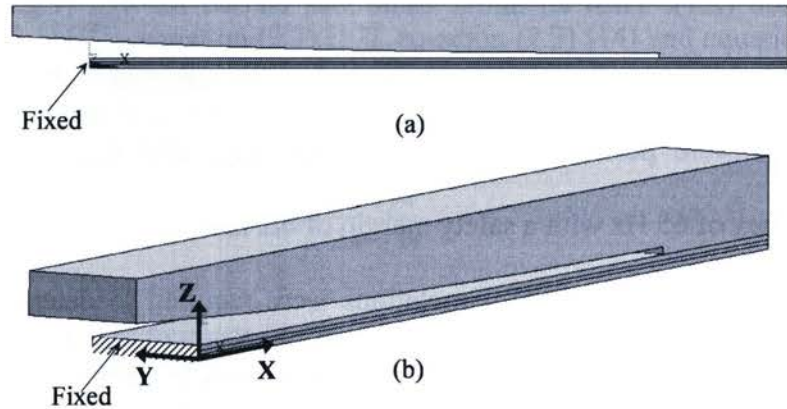


Figure 2.5 ANSYS model of curved L-shape mass harvester with base not shown.

The element type used for the two PZT layers, shim layer and curved L-shape mass volumes was Brick 8 node 45 element. The volumes were glued together to complete the 3D model. Mesh Tools was used to apply the mesh and properties of PZT, brass shim,

and tungsten proof mass to the 3D model. Block mesh from 0.1 mm to 1 mm was tested and it was found that a 1 mm block mesh was sufficient to obtain accurate results. The mesh size of 1 mm and properties given in Table 2.1 were applied to the model (see Figure 2.6). The cross-section of the beam at the boundary condition was fixed (see Figure 2.5a). Then the fundamental frequency was determined by solving the modal analysis using subspace mode extraction method. The fundamental mode shape data was obtained from the nodal displacements. For structural free vibration analysis, only the mechanical properties were needed, not the piezoelectric properties.

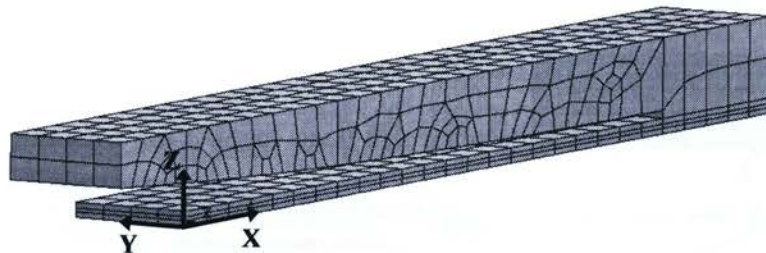


Figure 2.6 ANSYS model of curved L-shape mass harvester with mesh.

2.2.3 Procedure For Designing the Curved L-shape Mass Harvester

The completion of the curved L-shape mass harvester begins with finalizing the flat L-shape harvester. Then the flat mass bottom surface is converted into a curved mass bottom surface. The design procedure of the power harvester is given below.

1. Estimation of reference h_{mass} for ANSYS simulations

Using equations (2.1) – (2.4), an initial h_{mass} was estimated for the ANSYS simulations.

2. Determination of actual h_{mass}

A 3D model of the flat L-shape mass harvester with the reference h_{gap} and h_{mass} was simulated in ANSYS (see Figure 2.7). Using the modal analysis tool, the fundamental

frequency of the system was determined. If the simulated frequency did not match the designed frequency of 65 Hz, then the design variable h_{mass} was adjusted using equation 2.5, i.e., increasing or decreasing the mass of the system, until a frequency of $65 \text{ Hz} \pm 0.2 \text{ Hz}$ was achieved. Hence, a new reference h_{mass} was obtained. Then the nodal displacement results were recorded and these results were matched with the 3D model through the node numbers (see Figure 2.7b). Only the nodes of the beam and mass in the XZ plane were used in the data processing and they are shown in Figure 2.8.

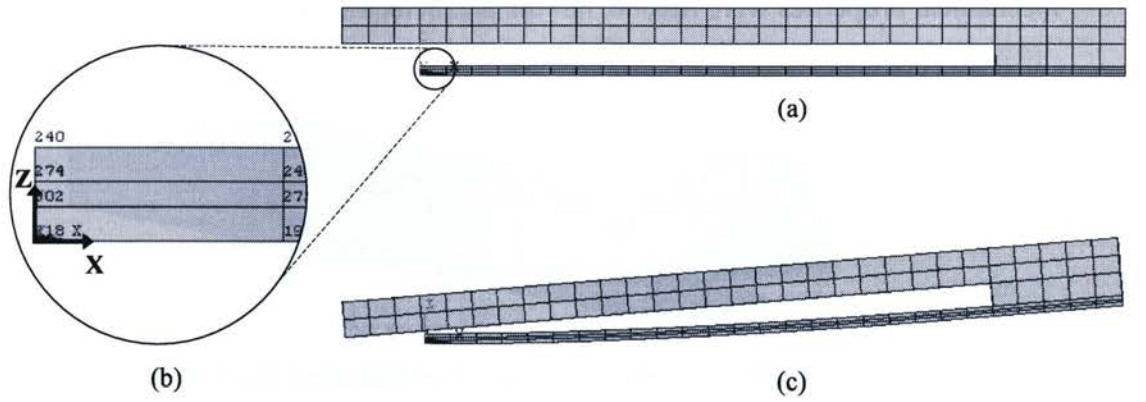


Figure 2.7 ANSYS model of a flat L-shape mass, (a) undeformed state and (b) node numbers in each element of the mesh and (c) deformed state showing the mode shape of the beam.

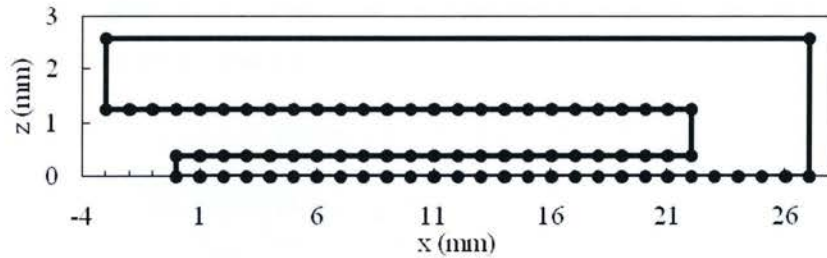


Figure 2.8 The beam and mass nodes used in the data processing of the simulation results.

3. Calculation of safety margin d_{safe}

The value of d_{safe} was calculated as the distance between points A and B in the deformed state (see Figure 2.3b). Using the nodal displacement results obtained in Step 2, d_{safe} was calculated based on a maximum beam tip displacement of 1 mm. If the

calculated d_{safe} did not match the designed d_{safe} of $0.2 \text{ mm} \pm 0.02 \text{ mm}$, then h_{gap} was adjusted using equation 2.6 such that d_{safe} equals to 0.2 mm (while keeping h_{mass} constant). Hence, a new reference h_{gap} was obtained and re-simulated in ANSYS to determine the new fundamental frequency. Then a new reference h_{mass} was calculated by using equation 2.7.

4. Finalization of h_{mass} and h_{gap}

Step 2 and step 3 were repeated until the values of h_{mass} and h_{gap} converge and result in a frequency of $65 \text{ Hz} \pm 0.2 \text{ Hz}$ and a d_{safe} of $0.2 \text{ mm} \pm 0.02 \text{ mm}$ respectively. The tolerance of 0.2 Hz and 0.02 mm were used because an accuracy of 20% of 1 unit was sufficient.

5. Conversion of finalized flat L-shape mass into a curved L-shape mass

The flat mass bottom surface of the finalized flat L-shape mass was then converted into a curve that followed the mode shape of the beam. Using the nodal displacement results obtained in Step 4, twenty six points on the mass bottom surface were shifted to follow the mode shape of the beam while maintaining a d_{safe} of 0.2 mm (see Figure 2.3c and Figure 2.3d). This curved L-shape mass has increased the mass of the system and changed the frequency and mode shape. Simulations in Steps 2 and 3 were repeated for the new curved L-shape mass harvester until the values of h_{mass} and h_{gap} converge and result in a frequency of $65 \text{ Hz} \pm 0.2 \text{ Hz}$ and a d_{safe} of $0.2 \text{ mm} \pm 0.02 \text{ mm}$ everywhere. The ANSYS simulation of the final curved L-shape mass design is shown in Figure 2.9. The results of intermediate steps are listed in Table 2.3 and the change in mass profile of flat L-shape mass to curved L-shape mass is shown in Figure 2.10. The final h_{mass} was determined to be 1.98 mm and the final gap between the mass and the beam varied from

0.2 mm ~ 0.84 mm respectively (see Figure 2.11). The final curved L-shape proof mass was 2.779 grams. The overall volume of the curved L-shape mass piezoelectric power harvester was 0.242 cm³. The steps of the procedure are summarized in a flow chart (see Figure 2.12).

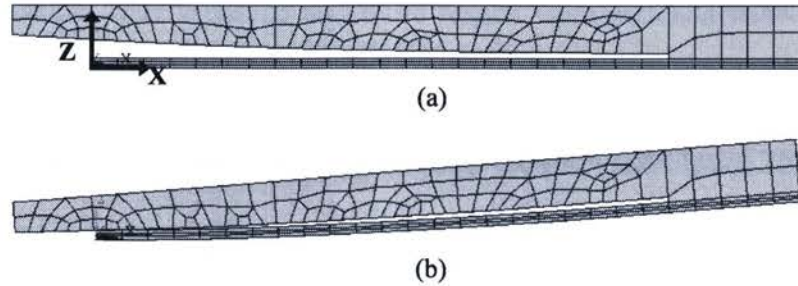


Figure 2.9 ANSYS model of the curved L-shape mass, (a) undeformed state and (b) deformed state showing the mode shape of the beam.

Table 2.3 Results of intermediate steps to the final curved L-shape mass design

Trial	h_{mass} (mm)	h_{gap} (mm)	m (g)	f (Hz)	d_{safe} (mm)
0	1.76	1.00	1.55	76.5	0.35
1	2.02	1.00	1.99	70.0	0.34
2	2.23	1.00	2.35	65.8	0.33
3	2.23	0.87	2.53	64.6	0.19
4	2.19	0.87	2.46	65.3	0.19
5	2.20	0.87	2.48	65.1	0.19
curved L-shape mass transformation					
6	2.20	0.2 - 0.88	3.12	61.6	0.20 - 0.22
7	2.08	0.2 - 0.86	2.94	63.4	0.20 - 0.20
8	1.97	0.2 - 0.86	2.75	65.3	0.20 - 0.20
9	1.99	0.2 - 0.86	2.79	64.9	0.20 - 0.20
10	1.98	0.2 - 0.84	2.779	65.1	0.20 - 0.20

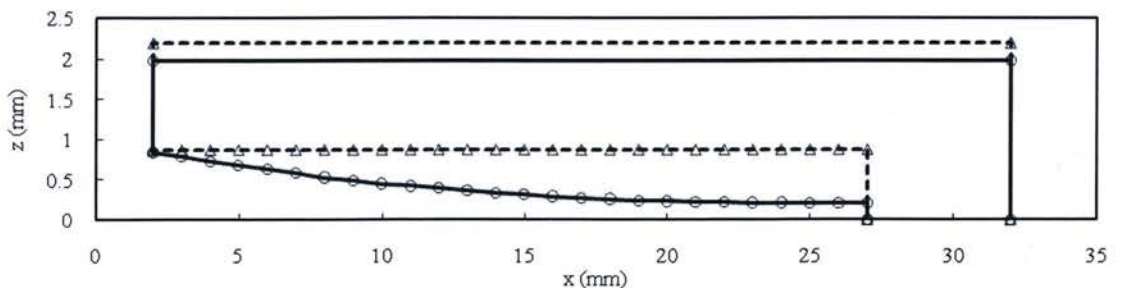


Figure 2.10 Change of mass profile from final flat L-shape to final curved L-shape.

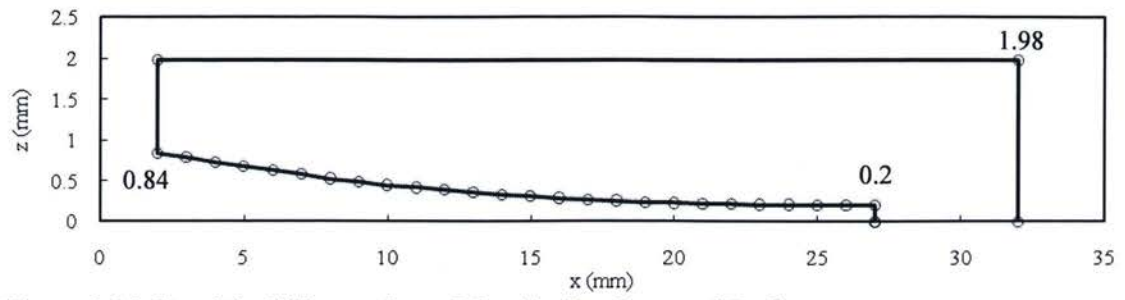


Figure 2.11 Graphical illustration of the finalized curved L-shape mass.

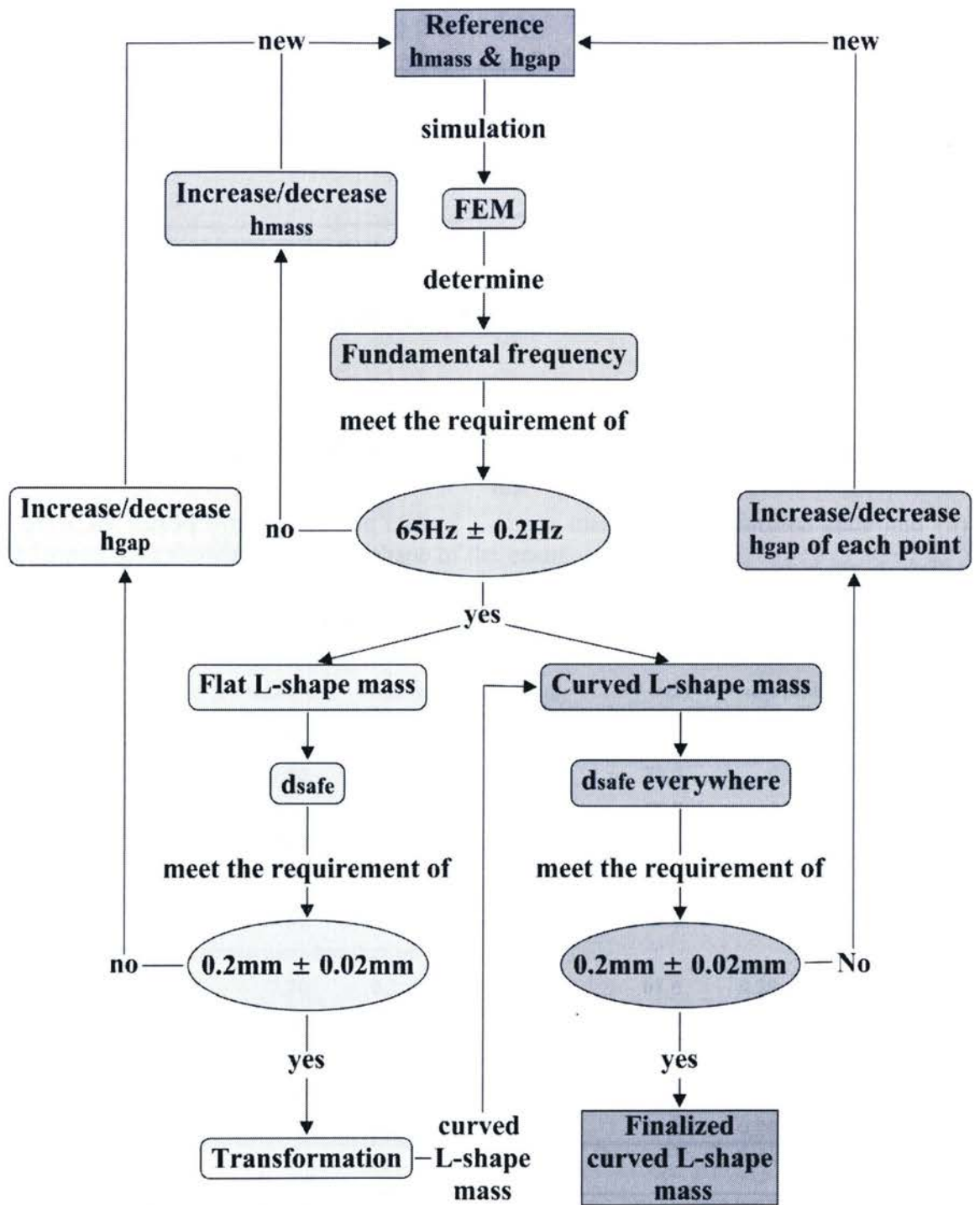


Figure 2.12 Flow chart for design of curved L-shape mass harvester.

Chapter 3: Comparison of Simulation Results of Curved L-Shape Mass Harvester With Conventional Mass Harvesters

The curved L-shape, block shape, and U-shape mass harvesters are compared based on two scenarios, i.e., 1) a fixed fundamental frequency, and 2) a fixed overall volume. For the first scenario, the different proof mass harvesters will result in different volume. For the second scenario, the different proof mass harvesters will result in different fundamental frequencies.

3.1 Fixed Fundamental Frequency

The design of the curved L-shape mass harvester in Chapter 2 has an overall volume of 0.242 cm^3 for a fixed fundamental frequency of 65 Hz. The volumes of the block shape mass and U-shape mass harvesters are determined when the fundamental frequency is fixed at 65 Hz.

3.1.1 Block Shape Mass Harvester

An example block mass harvester was designed using the same piezoelectric beam and tungsten proof mass material. The properties of the beam and mass are shown in Table 2.1 of Section 2.2.1. Using the same constraints as the curved L-shape mass harvester, i.e., 5 mm for base bonding (l_{base}), 5 mm for mass bonding (l_{mass}) and 22 mm for the free bending length (l_{bend}) (see Figure 3.1). The widths of the mass and the beam were 3.2 mm.

Iterations in ANSYS simulations were performed to achieve a fundamental frequency of 65 Hz. Equations (2.1)-(2.4) were used to estimate an initial h_{mass} for the ANSYS simulations. The h_{mass} was adjusted, which increased or decreased the mass of

the system, and re-simulated in ANSYS. Four iterations were required to achieve a fundamental frequency of 65.1 Hz. The ANSYS model of the block shape harvester is shown in Figure 3.2 and the results of intermediate steps are listed in Table 3.1. The final h_{mass} was determined to be 3.60 mm. The overall volume of the block mass harvester was 0.408 cm^3 .

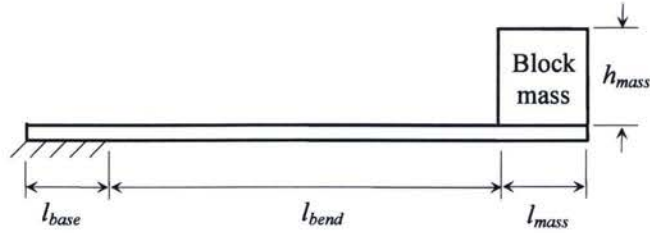


Figure 3.1 Schematic of a piezoelectric power harvester with a block shape mass.

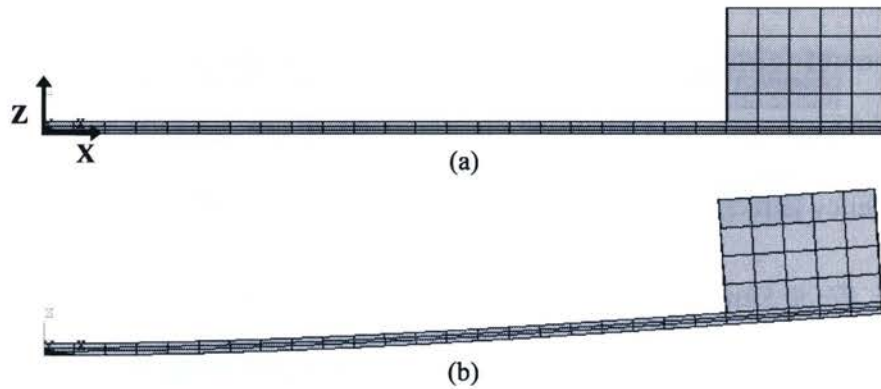


Figure 3.2 ANSYS model of the block shape mass harvester, (a) undeformed state and (b) deformed state showing the mode shape of the beam.

Table 3.1 Results of intermediate steps to a 65 Hz block shape mass harvester.

Trial	h_{mass} (mm)	m (g)	f (Hz)
0	5.54	1.55	52.7
1	4.24	1.19	60.2
2	3.41	0.95	66.9
3	3.64	1.02	64.8
4	3.60	1.01	65.1

3.1.2 U-Shape Mass Harvester

A U-shape mass, shown in Figure 3.3, was used in [15, 16]. The U-shape design consists of two gaps between the mass and beam. Similar to the flat L-shape mass (see Figure 2.3b), the space of two gaps between the beam and mass is not fully utilized to accommodate as much mass as possible.

The U-shape mass harvester was design using the same constraints as the curved L-shape mass harvester, i.e., 5 mm for base bonding (l_{base}), 5 mm for mass bonding (l_{mass}) and 22 mm for the free bending length (l_{bend}) (see Figure 3.3). Since the mass is symmetric, it cannot go beyond the bonding part of the beam and a mass length (l_{total}) of 27 mm was used instead of 30 mm used for the curved L-shape mass. The widths of the mass and the beam were 3.2 mm.

Iterations in ANSYS simulations were performed to achieve a fundamental frequency of 65 Hz. Equations (2.1)-(2.4) were used to estimate an initial h_{mass} for the simulations. The h_{mass} and h_{gap} were adjusted by following steps 1 to 4 of the procedure in Section 2.2 and three iterations were required to achieve a fundamental frequency of 65.1 Hz. The ANSYS model of the U-shape mass harvester is shown in Figure 3.4 and the results of intermediate steps are listed in Table 3.2. The h_{mass} and h_{gap} were determined to be 2.58 mm and 0.62 mm respectively. The overall volume of the U-shape harvester was 0.303 cm^3 .

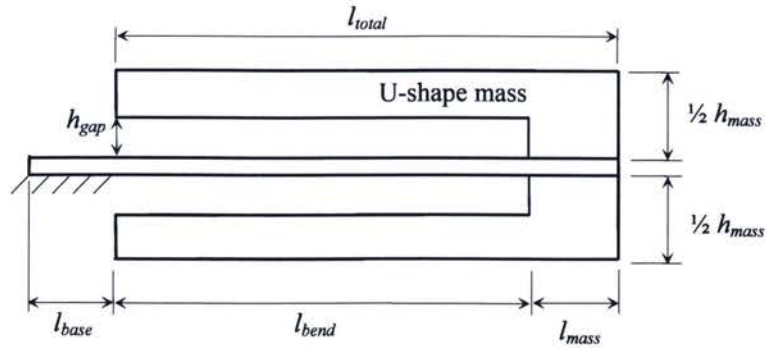


Figure 3.3 Schematic of a piezoelectric power harvester with a U-shape mass.

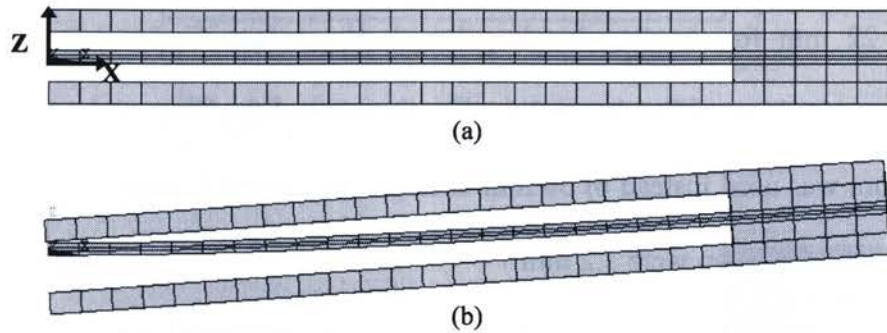


Figure 3.4 ANSYS model of the U-shape mass harvester, (a) undeformed state and (b) deformed state showing the mode shape of the beam.

Table 3.2 Results of intermediate steps to a 65 Hz U-shape mass harvester.

Trial	h_{mass} (mm)	h_{gap} (mm)	m (g)	f (Hz)	d_{safe} (mm)
0	2.66	1.00	1.55	69.3	0.58
1	2.66	0.63	2.47	64.0	0.21
2	2.59	0.62	2.40	64.8	0.20
3	2.58	0.62	2.37	65.1	0.20

3.1.3 Comparison of Different Proof Mass Harvesters With Fixed Fundamental Frequency

The simulation results of the curved L-shape mass (from Chapter 2 Section 2.2.3), block shape mass, and U-shape mass power harvesters are summarized in Table 3.3. The results showed that for a fixed fundamental frequency of 65 Hz, the volume of the curved L-shape mass harvester (0.242 cm^3) was 69% and 25% smaller than the volume of block

shape mass harvester (0.408 cm^3) and U-shape mass harvester (0.303 cm^3) respectively. For applications of high input vibration, e.g., real-time pressure monitoring inside car tires, the three different mass shape harvesters can all reach the maximum allowed tip displacement of 1 mm, which is determined by the composite beam strength and free bending length (see Figure 3.5). Therefore, the three harvesters will have the same output power because they have the same fundamental frequency and approximately the same mode shape.

Thus, for the same fundamental frequency of 65 Hz, the curved L-shape mass harvester can achieve a power density that is 69% and 25% higher than that of block shape and U-shape mass harvesters respectively.

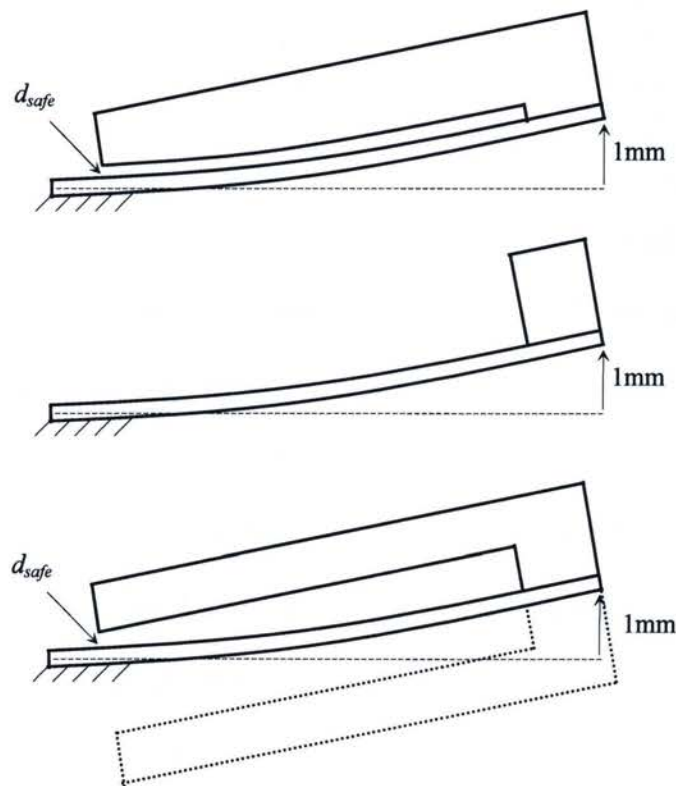
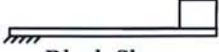




Figure 3.5 Maximum allowed tip displacement of: (a) curved L-shape mass harvester, (b) block shape mass harvester and (c) U-shape mass harvester.

Table 3.3 Simulation results of different proof mass power harvester with 65 Hz fundamental frequency.

Designs	l_{base} (mm)	l_{bend} (mm)	l_{mass} (mm)	w (mm)	l_{total} (mm)	h_{beam} (mm)	h_{gap} (mm)	h_{mass} (mm)	\forall (cm ³)	f (Hz)
 Block Shape	5	22	5	3.2	5	0.38	-	3.60	0.408	65.1
 U-Shape	5	22	5	3.2	27	0.38	0.62	2.58	0.303	65.1
 Curved L-Shape	5	22	5	3.2	30	0.38	0.2~0.84	1.98	0.242	65.1

3.2 Fixed Overall Volume

The design of the curved L-shape mass harvester in Chapter 2 has a fundamental frequency of 65 Hz for a fixed overall volume of 0.242 cm³. The fundamental frequency of the block shape mass and U-shape mass harvesters are determined when the overall volume is fixed at 0.242 cm³.

3.2.1 Block Shape Mass Harvester

An example block shape mass harvester with an overall volume of 0.242 cm³ was designed using the same piezoelectric beam and tungsten proof mass material. The properties of the beam and mass are shown in Table 2.1 of Section 2.2.1. The same constraints as the curved L-shape mass harvester, i.e., 5 mm for base bonding (l_{base}), 5 mm for mass bonding (l_{mass}), 22 mm for the free bending length (l_{bend}), and 3.2 mm for the width of beam and mass were applied to the block shape harvester (see Figure 3.1).

Based on the fixed volume of 0.242 cm³, the h_{mass} was calculated to be 1.98 mm. The block shape proof mass was determined to be 0.554 grams and the fundamental frequency of the block shape mass harvester was simulated to be 85.7 Hz.

3.2.2 U-Shape Mass Harvester




An example U-shape mass harvester with a volume of 0.242 cm^3 was designed using the same piezoelectric beam and tungsten proof mass material. The constraints of 5 mm for base bonding (l_{base}), 5 mm for mass bonding (l_{mass}), 22 mm for the free bending length (l_{bend}), 27 mm for mass length (l_{total}) and 3.2 mm for the width of beam and mass were applied to the U-shape harvester (see Figure 3.3).

Based on the fixed volume of 0.242 cm^3 , the h_{mass} was calculated to be 1.98 mm and h_{gap} was determined to be 0.63 mm in ANSYS. The U-shape proof mass was determined to be 1.442 grams. The fundamental frequency of the U-shape mass power harvester was simulated to be 76.7 Hz.

3.2.3 Comparison of Different Mass Harvesters With Fixed Overall Volume

The simulation results of the curved L-shape mass (from Chapter 2 Section 2.2.3), block shape mass, and U-shape mass power harvesters are summarized in (see Table 3.4). The results showed that for a fixed overall volume of 0.242 cm^3 , the fundamental frequency of curved L-shape mass harvester (65.1 Hz) was 24% and 15% lower than that of the block shape (85.7 Hz) and U-shape (76.7 Hz) mass harvesters respectively. Hence, the curved L-shape mass harvester is more suitable for many practical applications such as harvesting human body movement and rotating machinery, which always have low frequency vibrations. The curved L-shape mass design (2.779 grams) has 400% and 93% more mass than the block shape (0.554 grams) and U-shape mass (1.442 grams) designs respectively. Since more mass means more generated power for a given input vibrations, the curved L-shape mass can generate the highest power density.

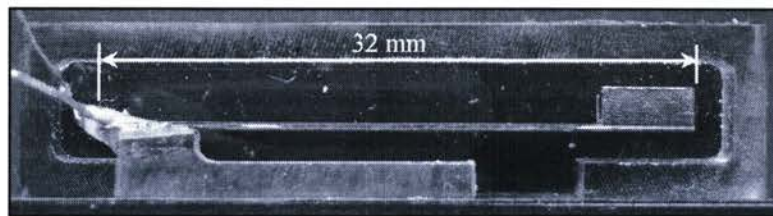
Table 3.4 Simulation results of different proof mass power harvester with 0.242 cm^3 fixed overall volume.

Designs	w (mm)	l_{total} (mm)	h_{gap} (mm)	h_{mass} (mm)	Ψ (cm^3)	Mass (grams)	f (Hz)
 Block Shape	3.2	5	-	1.98	0.242	0.554	85.7
 U-Shape	3.2	27	0.63	1.98	0.242	1.442	76.7
 Curved L-Shape	3.2	30	0.2~0.84	1.98	0.242	2.779	65.1

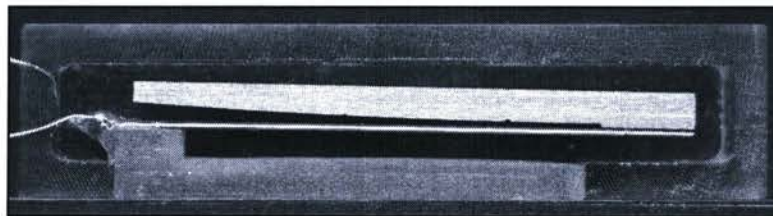
Chapter 4: Fabrication and Assembly of Prototypes

The fabrication and assembly procedure presented in this chapter were developed based on trial and error of more than ten successful and unsuccessful prototypes. The result is a procedure that can produce robust prototypes with high success rates.

Four piezoelectric power harvester prototypes, using a baseline power harvester volume of 0.242 cm^3 , were fabricated and assembled; three curved L-shape mass prototypes and one block shape mass prototype (see Figure 4.1). The components of each power harvester include a Tungsten proof mass, a PZT composite beam, a base and a casing (see Figure 4.2).



(a)



(b)

Figure 4.1 Piezoelectric power harvester prototype with, (a) Tungsten block shape mass and (b) Tungsten curved L-shape mass.

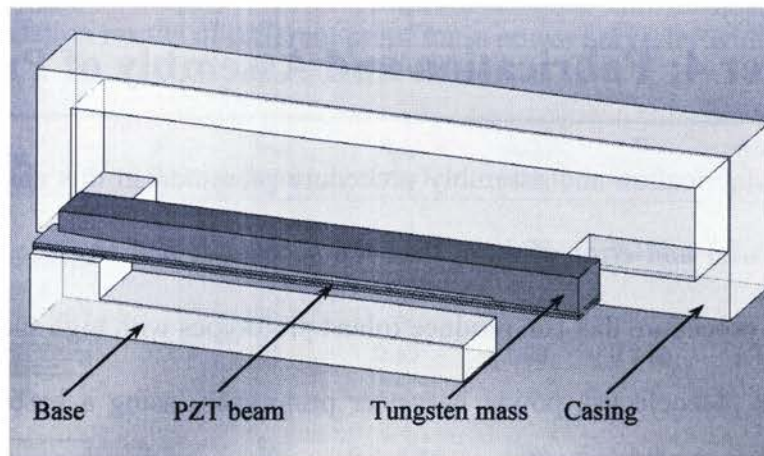


Figure 4.2 Components of the piezoelectric power harvester prototype.

4.1 Tungsten Proof Mass

The proof mass is tungsten nickel alloy and the raw material was purchased from Federal Carbide Company. The tungsten nickel alloy has a very high density (17.5 g/cm^3) compared with steel of 7.8 g/cm^3 and lead of 11.35 g/cm^3 . A denser material for the proof mass is always more advantageous because more mass can be included in a given volume. Thus, a power harvester that has a denser proof mass can incorporate more mass for a given volume, which lowers the fundamental frequency and produces more power.

As shown in Figure 4.3, the shape of the curved mass profile was cut out using wired electrical discharge machining (EDM) (LP Precision Form Tools Ltd) to achieve the required accuracy of 0.01mm . The exact coordinates of the curved and block mass profiles are shown in Figure 4.4 and the number above each point indicate the vertical position of the point.

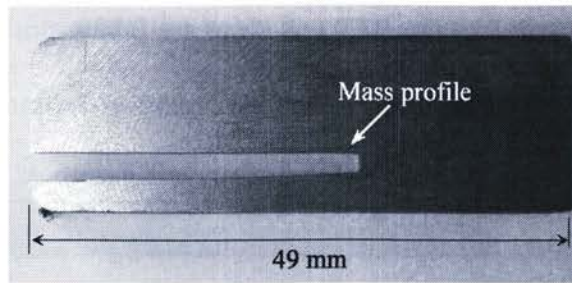


Figure 4.3 Wire EDM profile of the Tungsten proof mass in the raw material.

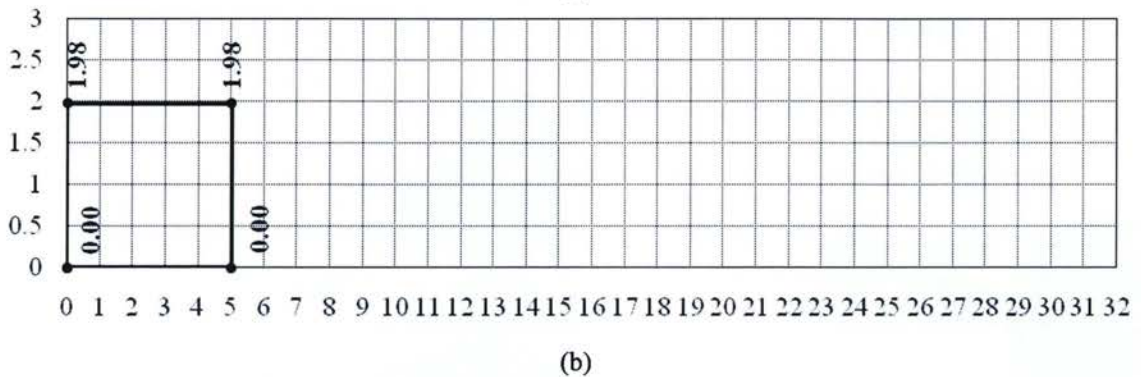
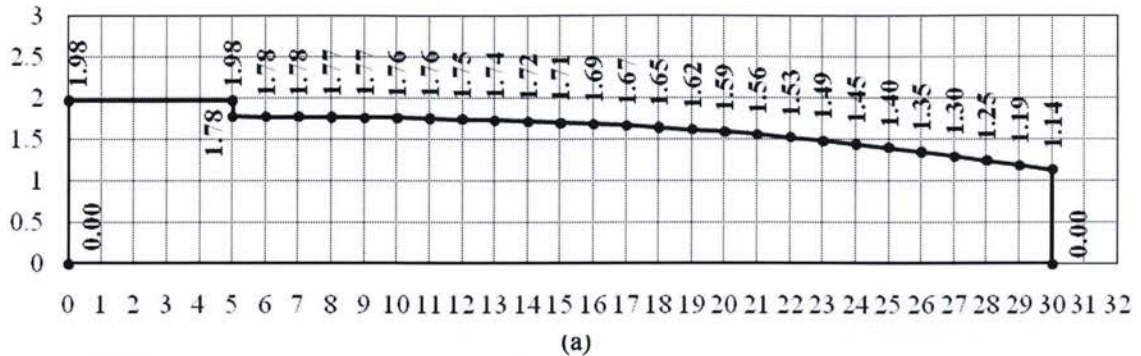


Figure 4.4 Graphical illustration of (a) curved L-shape mass profile and (b) block shape mass profile. All dimensions are in millimeters.

4.2 Bimorph Piezoelectric Beam

The bimorph PZT piezoelectric beam was purchased from Piezo Systems Inc. (T215-H4-103Y [59], see Figure 4.5). It consisted of two PZT layers that were sandwiched onto a brass center shim (see Figure 4.6). The addition of the brass shim layer improves the strength of the beam. The top and bottom surface of the beam has a very thin layer of nickel, which acts as an electrode, to collect the charges produced by

the PZT. The thickness of the PZT and shim are 0.139 mm and 0.102 mm respectively. The length and width of the entire beam is 32 mm and 3.2 mm respectively.

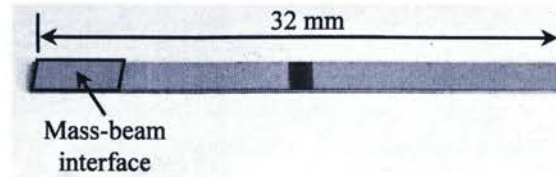


Figure 4.5 Piezoelectric composite beam (T215-H4-103Y).

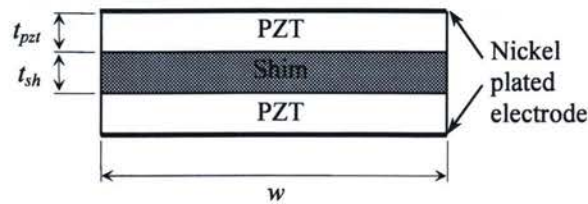


Figure 4.6 Schematic of the PZT composite beam cross-section.

There are two methods to connect the PZT beam (series connection and parallel connection). When the two PZT layers are connected as Figure 4.7a, the top and bottom layer are in series because the voltage produced by each layer will add. When the two PZT layers are connected as Figure 4.7b, the top and bottom layer are in parallel because the current produced by each layer will add. Connecting the beam in series or parallel only changes the voltage to current ratio and it does not change the power output. For the prototypes in this thesis, the PZT beams were connected in parallel.

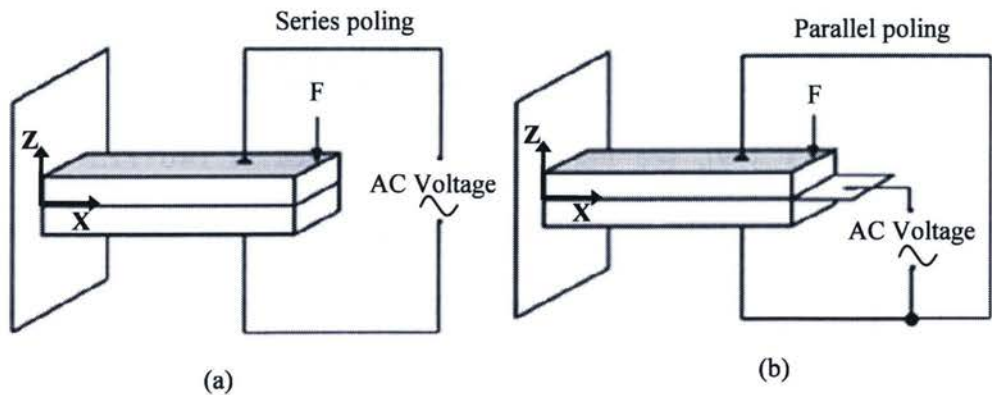


Figure 4.7 Connections of the piezoelectric beam in (a) series and (b) parallel.

The procedure to prepare the beam for parallel connection is as follows. First an area of the brass shim was exposed by removing an area of the top PZT layer (see Figure 4.8a). The beam was held on a flat surface with double sided tape. The flat surface will ensure that the beam does not bend and break during the machining process. The area to be removed (approx. $1.5 \text{ mm} \times 1.5 \text{ mm}$) was marked with a black marker. Use of pencil is not recommended as it may scratch off the electrode or damage the material. Using a hand-held Dremel tool with a grinding bit shown in Figure 4.8b, the marked PZT area was removed with a few passes. The hand-held Dremel worked because the hand can feel and control the force applied and PZT material of only 0.139 mm thick was easily removed without damaging the shim. After exposing the shim, the beam was removed by slowly peeling off the tape along the width direction.

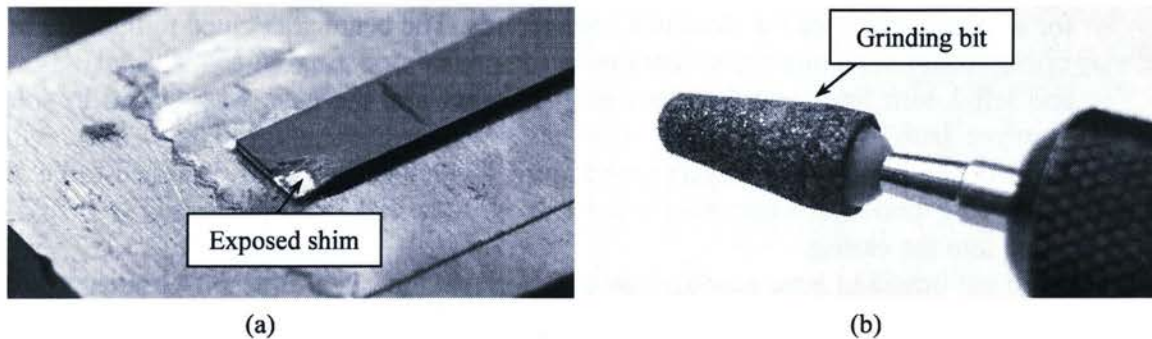


Figure 4.8 (a) Exposed shim area of the piezoelectric beam and (b) Grinding bit used to expose the shim.

The nickel electrode at the interface of the PZT beam and proof mass was removed to prevent short circuiting (see Figure 4.5). Using fine sandpaper, approximately $5 \text{ mm} \times 3.2 \text{ mm}$ of the electrode at the tip of the beam was removed and the colour of the surface changes from light grey to dark grey. A multi-meter was used to ensure that the sandpapered part was not connected to the rest of the beam.

4.3 Base and Casing

The base and casing were both made of clear polycarbonate plastic and they were CNC machined to the specifications shown in Figure 4.9 and Figure 4.10. The base was designed to be L-shaped (4 mm tall, 25 mm long, and 5 mm wide) for several reasons. First, the L-shaped base allowed the cantilever power harvester to stand on its own, which improved handling of the power harvester during assembly. Second, the 4 mm height allowed for 2 mm clearance between the PZT beam and casing to compensate for any assembly errors. Third, the 25 mm base was 7 mm shorter than the beam, which left enough room for clamping the proof mass to the beam (see Figure 4.12b). Finally, the width of the base was 5 mm, which was 1.8 mm wider than the beam, because after the beam was glued onto the base, the base can be clamped (instead of clamping the beam) for soldering the wire for electrical connections. The beam was glued onto the base at 5 mm and left 1 mm free (interface between the beam and the base was 4 mm) to solder the wire for the bottom PZT layers (see Figure 4.11). The base was designed to be slid and glued into the casing.

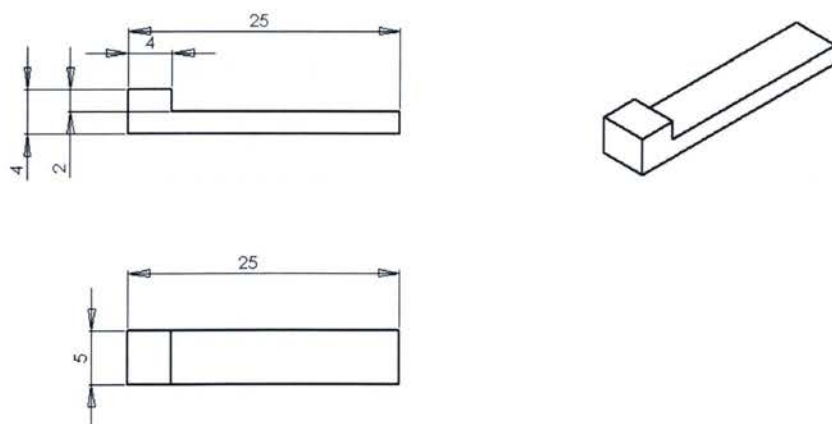


Figure 4.9 CAD drawing of the base (dimensions are in millimeters).

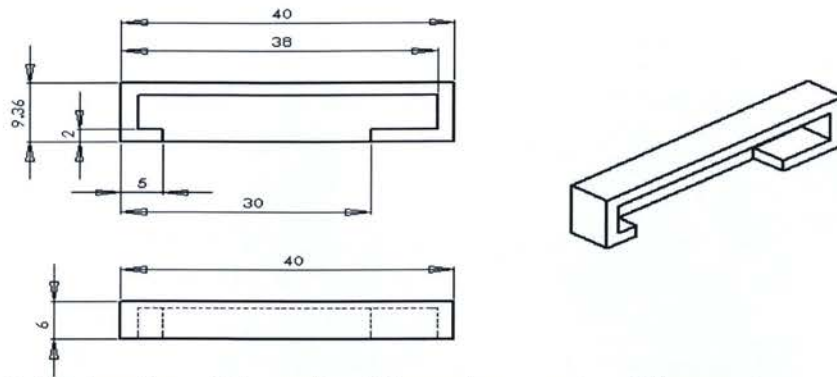


Figure 4.10 CAD drawing of the casing (dimensions are in millimeters).

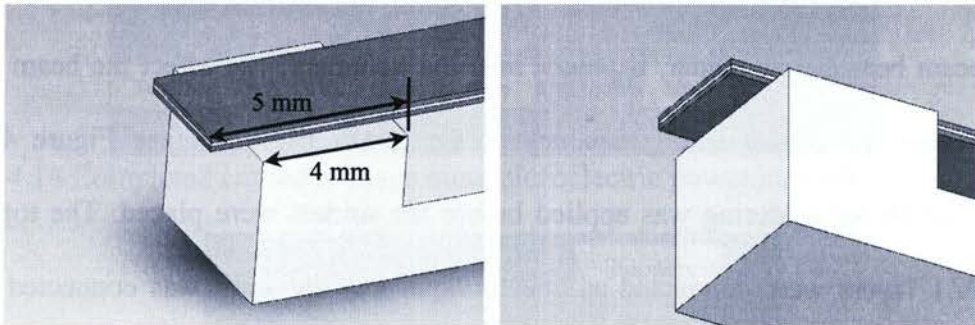


Figure 4.11: Attachment of the beam to the base.

The PZT beam, base, and mass were assembled to complete the piezoelectric power harvester. The beam was glued onto the base using LOCTITE dual syringe epoxy (E20HP). The epoxy was applied to the beam and base and any excess glue was cleaned away using Q-tips and Isopropyl alcohol. Then a vice was used to clamp the beam to the base. Because the vice has a hard metallic surface, a piece of plastic was placed between the vice and the PZT beam to avoid damaging the PZT (see Figure 4.12a). The beam was clamped to the base for 24 hours to allow the epoxy to cure properly. The mass was clamped to the PZT beam by following the same procedure (see Figure 4.12b).

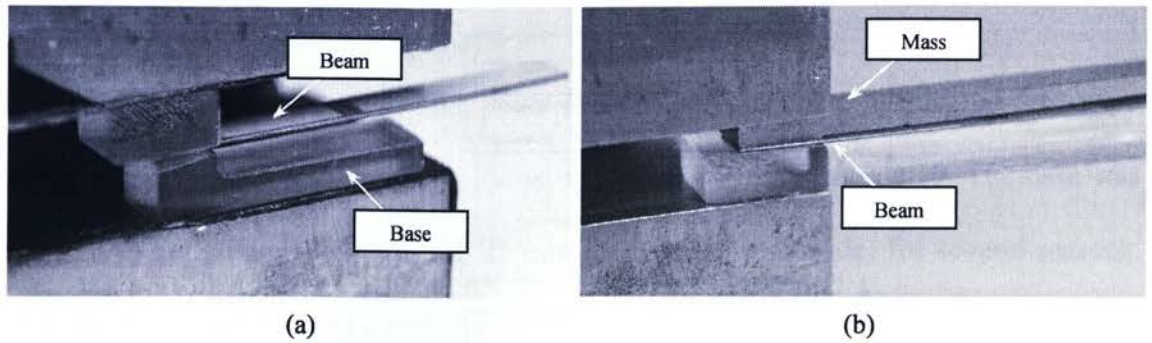


Figure 4.12 Clamping the piezoelectric beam to (a) plastic base and (b) mass.

The electrical connections of the PZT beam were soldered at the fixed end of the beam because the solder, if placed near the boundary, can affect the beam stiffness and change the fundamental frequency of the power harvester (see Figure 4.13). A flux solution for soldering was applied before the solders were placed. The top and bottom PZT layers were connected as one terminal and the shim was connected as the other terminal (see Figure 4.13). Then epoxy was applied over the solder to permanently secure the connections.

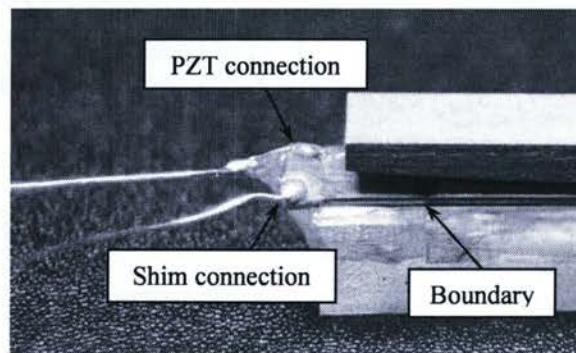


Figure 4.13 Soldered connections of the power harvester.

A working prototype of the power harvester was completed (see Figure 4.14). For practical applications, it is important to limit the tip displacement of the power harvester to avoid failure of the beam. The input accelerations can be very high and cause the power harvester to bend beyond its limit. The tip displacement of the power harvester was confined to 1 mm with the help of the casing and stoppers (see Figure 4.15). The

stoppers were built with many layers of tape. The same procedure was repeated for the three curved L-shape mass prototype and the block shape mass prototype (see Figure 4.1a and Figure 4.1b.)

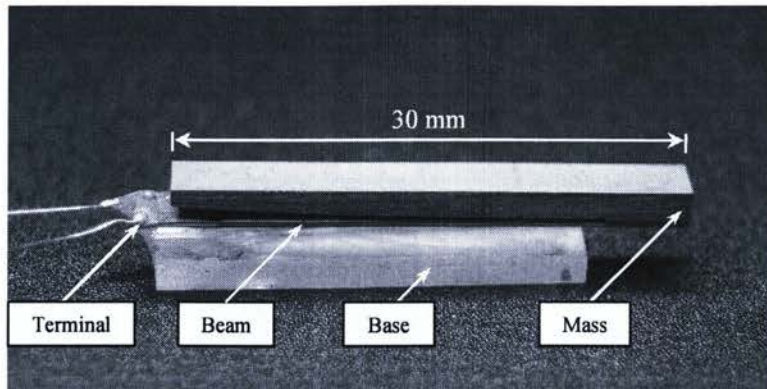


Figure 4.14 Completed curved L-shape mass piezoelectric power harvester.

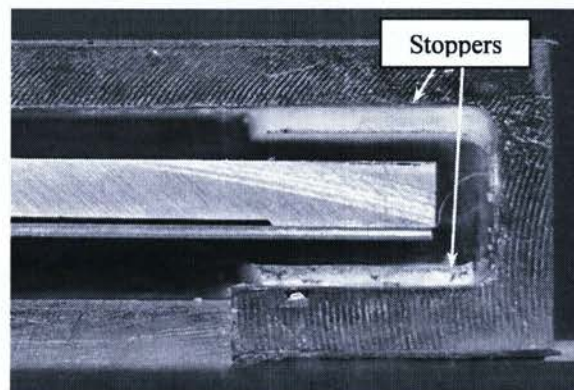


Figure 4.15 Limiting the tip displacement of using the casing and stoppers.

Chapter 5: Experimental Testing on a Shaker

The three curved L-shape and the block shape mass power harvester prototypes are tested on a standard shaker (VTS VG-100) (see Figure 5.1). The fundamental frequency and power output of each power harvester are measured by performing a frequency sweep from 10 to 120 Hz at input accelerations of 0.25 g to 0.75 g. Each power harvester is individually tested on the shaker without the casing because the input acceleration can be controlled.

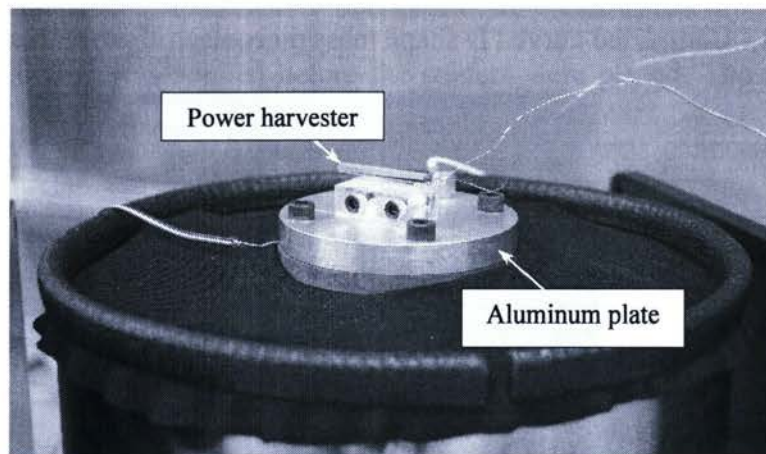


Figure 5.1 Setup of the power harvester on the shaker.

5.1 Setup of the Shaker Experiment

The complete setup of the shaker experiment is shown in Figure 5.2. The shaker control software was used to increase/decrease the output frequency and acceleration of the shaker. The output terminals of the power harvester were connected to the oscilloscope and data acquisition card (DAC). The oscilloscope displayed the voltage signal in real-time and the DAC recorded the output signal into data files. The settings used for the DAC was 5,000 samples/second and 10,000 samples were obtained for each measurement. The DAC hardware resolution used was 16 bits, which ensures that the

dynamic range was high enough to detect small signals in the presence of large signals. A block diagram of the equipments setup is shown in Figure 5.3. The shaker supplied a sinusoidal base excitation of a set frequency and acceleration to the power harvester. The output of the power harvester was AC voltage that was measured by the DAC.

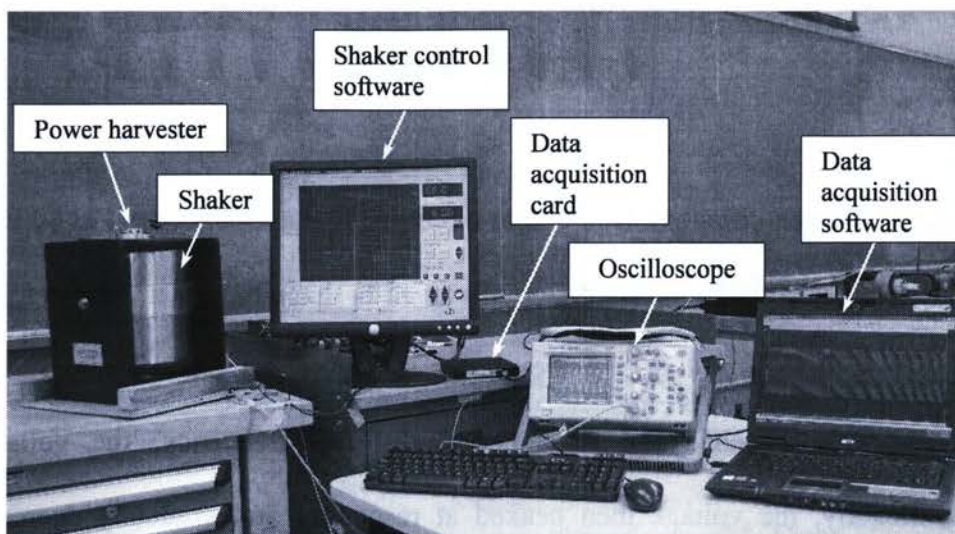


Figure 5.2 Complete setup of the shaker experiment.

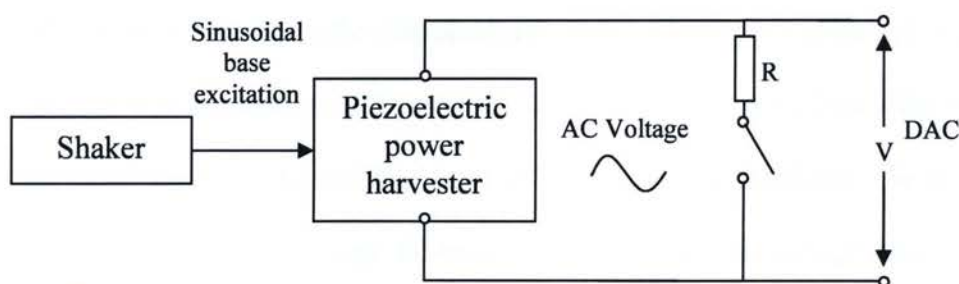


Figure 5.3 Block diagram of the setup of the shaker experiment.

5.2 Shaker Test Results of Curved L-Shape Power Harvester 1, 2 and 3

5.2.1 Fundamental Frequency of Curved L-Shape Mass Harvester

The fundamental frequency of each curved L-shape mass harvester was determined by measuring the open-circuit voltage output of the harvester from 10 to 120 Hz. An open-circuit voltage measurement of curved L-shape harvester 1 for 60 Hz @ 0.75 g is shown in Figure 5.4 and the signal is AC voltage of approximately ± 16 V.

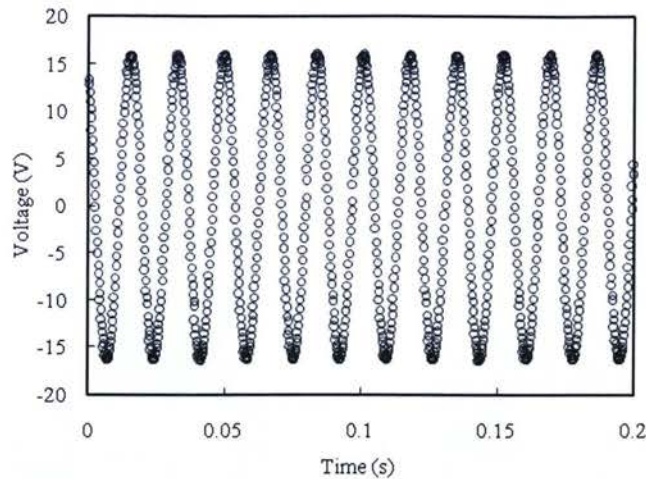


Figure 5.4 Open-circuit voltage output of curved L-shape harvester 1 at 60 Hz @ 0.75 g.

The peak open-circuit voltage of curved L-shape harvester 1 from 55 Hz to 75 Hz at 0.25 g, 0.55 g and 0.75 g are shown in Figure 5.5 (solid lines). When the input frequency approached the fundamental resonant frequency, the voltage increased significantly, the voltage then peaked at resonance and gradually decreased as input frequency moved away from the resonant frequency. For example, at 0.75 g of curved L-shape harvester 1 in Figure 5.5 (solid line), the voltage increased from 7.88 V @ 58.5 Hz to 11.6 V @ 59 Hz and to 15.3 V @ 59.5 Hz. The voltage reached the maximum of 16.0 V at the fundamental frequency of 60 Hz. Then the voltage dropped as the input frequency increased and moved away from 60 Hz.

The measured fundamental frequency decreased with increasing input acceleration. As shown in Figure 5.5, the fundamental frequencies of curved L-shape harvester 1 were 63.5 Hz, 61.0 Hz and 60.0 Hz when the input accelerations were 0.25 g, 0.55 g and 0.75 g respectively (solid lines). The fundamental frequencies of curved L-shape harvester 2 were 72.5 Hz, 71 Hz and 69.5 Hz when the input accelerations were 0.25 g, 0.50 g and 0.75 g respectively (dotted lines). The fundamental frequencies of curved L-shape harvester 3 were 65.5 Hz, 64.0 Hz and 63.0 Hz when the input accelerations were 0.25 g,

0.50 g and 0.75 g respectively (dash lines). The change in fundamental frequency with input acceleration is attributed to the electro-mechanical properties of the piezoelectric beam.

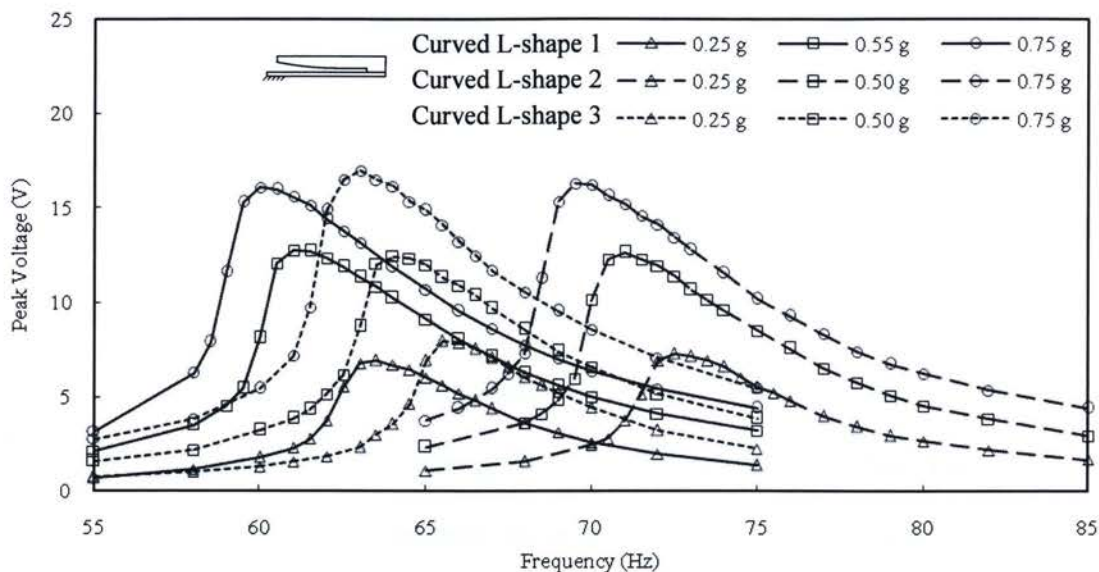


Figure 5.5 Peak open-circuit voltage versus frequency of curved L-shape harvester 1, 2 and 3 at different input accelerations.

5.2.2 Power Output of Curved L-Shape Mass Harvester

The power output of each curved L-shape mass harvester was determined by measuring the voltage output at different resistive loads for a frequency sweep of 10 to 120 Hz. An example of the voltage measurement, when curved L-shape harvester 1 was connected to 80 k Ω at an input of 60.5 Hz @ 0.75 g, is shown in Figure 5.6. The measured signal was AC voltage of approximately ± 7.6 V. The RMS value of the AC voltage was used to calculate the average power output of the curved L-shape harvesters.

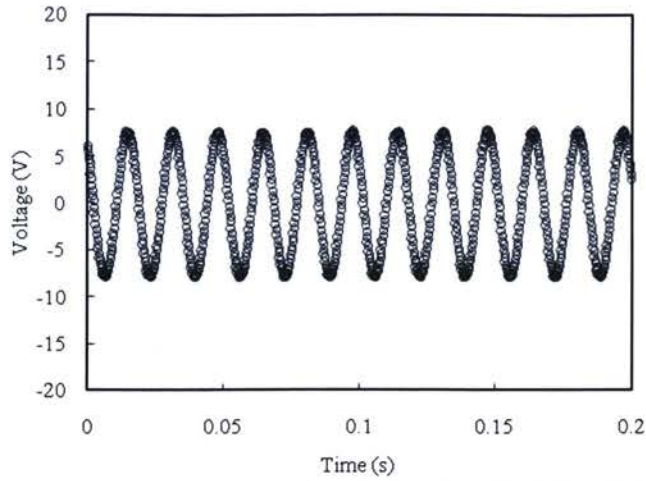


Figure 5.6 Voltage measurement of curved L-shape 1 at 60.5 Hz @ 0.75 g for a resistive load of 80 k Ω .

The voltage versus frequency of curved L-shape 1, 2 and 3 for different resistive loads at a fixed input acceleration of 0.75 g are shown in Figure 5.7. The peak voltage increased with increasing resistive loads. For curved L-shape harvester 1, the peak voltage of 30 k Ω , 80 k Ω , 200 k Ω and 500 k Ω curves were measured to be 4.3 V, 7.6 V, 11.2 V and 13.9 V respectively (see Figure 5.7a). For curved L-shape harvester 2, the peak voltage of 40 k Ω , 100 k Ω , 300 k Ω and 500 k Ω curves were measured to be 5.2 V, 8.4 V, 12.6 V and 13.8 V respectively (see Figure 5.7b). For curved L-shape harvester 3, the peak voltage of 40 k Ω , 117 k Ω , 300 k Ω and 500 k Ω were measured to be 5.3 V, 9.3 V, 12.8 V and 14.1 V respectively (see Figure 5.7c).

The resonant frequency of the power harvesters (input frequency that matches the natural frequency of the system) varied at different resistive loads. For curved L-shape harvester 1, the resonant frequencies at 30 k Ω , 80 k Ω , 200 k Ω and 500 k Ω were measured to be 58.5 Hz, 60.5 Hz, 61.0 Hz and 60.5 Hz respectively (see Figure 5.7a). For curved L-shape harvester 2, the resonant frequencies at 40 k Ω , 100 k Ω , 300 k Ω and 500 k Ω were measured to be 69.0 Hz, 70.5 Hz, 70.5 Hz and 70.5 Hz respectively (see Figure

5.7b). For curved L-shape harvesters 3, the resonant frequencies at 40 k Ω , 117 k Ω , 300 k Ω and 500 k Ω were measured to be 62.0 Hz, 64.0 Hz, 64.0 Hz and 63.5 Hz respectively (see Figure 5.7c). The variation of resonant frequency with different resistive loads is attributed to the extra electrical damping induced on the power harvester system by the resistive loads.

The power versus frequency for curved L-shape harvester 1, 2 and 3 at different resistive loads for a fixed input acceleration of 0.75 g are shown in Figure 5.8. For curved L-shape harvester 1, the highest power output was measured at 80 k Ω with 60.5 Hz resonant frequency (see Figure 5.8a). For curved L-shape harvester 2, the highest power output was measured at 100 k Ω with 70.5 Hz resonant frequency (see Figure 5.8b). For curved L-shape harvester 3, the highest power output was measured at 117 k Ω with 64.0 Hz resonant frequency (see Figure 5.8c).

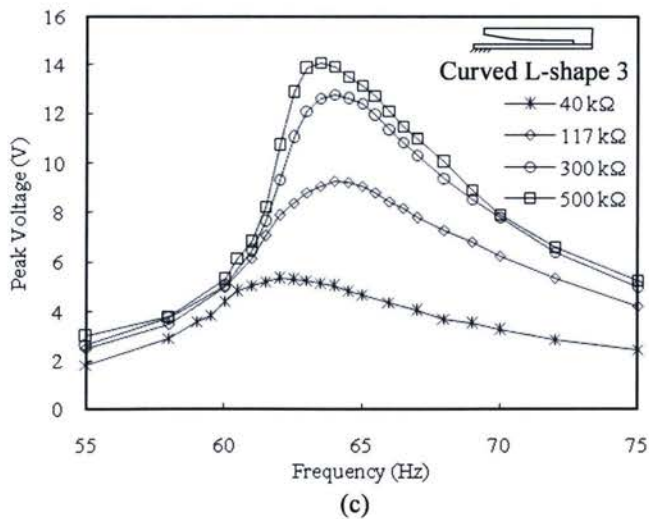
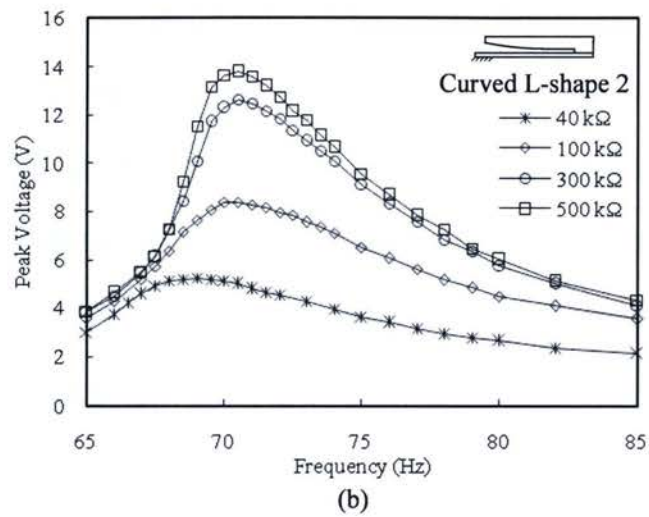
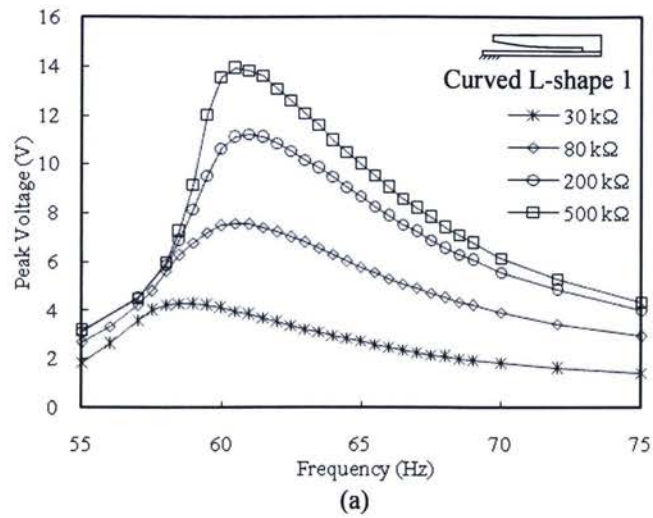
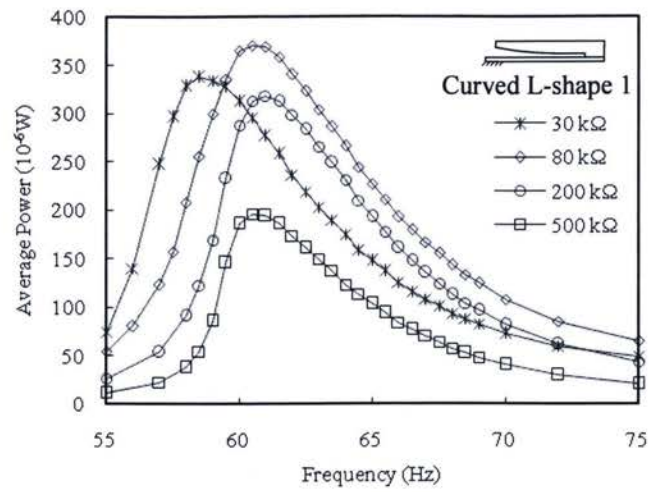
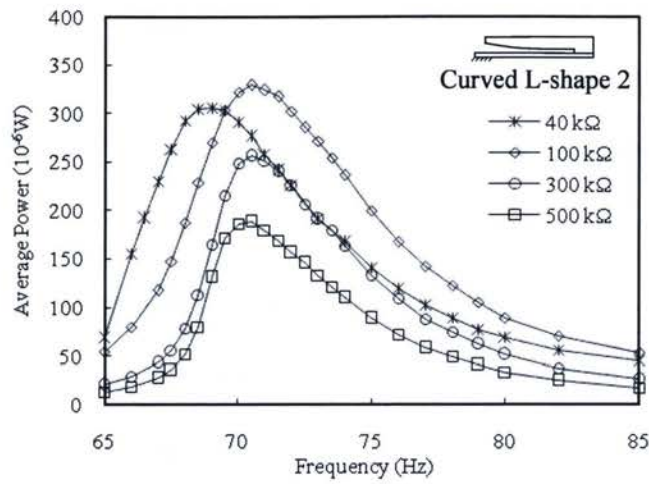


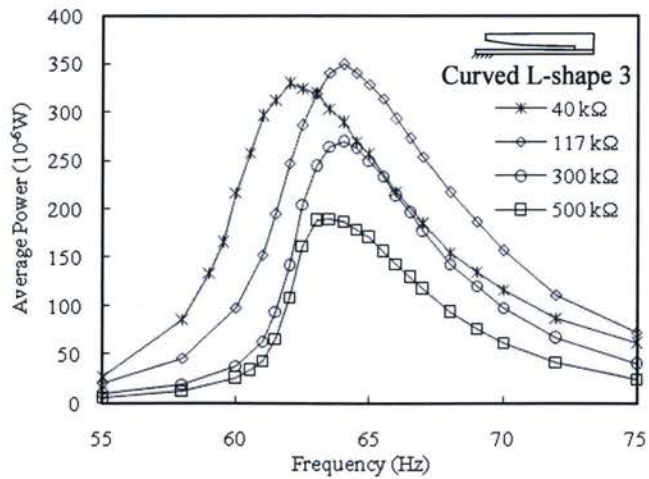
Figure 5.7 Voltage versus frequency at different resistive loads for a fixed input acceleration of 0.75 g. (a) curved L-shape harvester 1, (b) curved L-shape harvester 2 and (c) curved L-shape harvester 3.



(a)



(b)



(c)

Figure 5.8 Power versus frequency of different resistive loads for a fixed input acceleration of 0.75 g. (a) curved L-shape harvester 1, (b) curved L-shape harvester 2 and (c) curved L-shape harvester 3.

The voltage versus resistive load for curved L-shape harvester 1, 2 and 3 at a fixed input acceleration of 0.75 g are shown in Figure 5.9. The voltage increased with increasing resistive load. For curved L-shape harvester 1, the voltage increased from 3.0 V to 13.9 V when the resistive load increased from 20 k Ω to 500 k Ω (see Figure 5.9 solid line). For curved L-shape harvester 2, the voltage increased from 3.0 V to 13.8 V when the resistive load increased from 20 k Ω to 500 k Ω (see Figure 5.9 dotted line). For curved L-shape harvester 3, the voltage increased from 3.1 V to 13.9 V when the resistive load increased from 20 k Ω to 500 k Ω (see Figure 5.9 dash lines).

The power output versus resistive load of curved L-shape harvester 1, 2 and 3 are shown in Figure 5.10. For curved L-shape harvester 1, the maximum power output was 371 μ W at the optimal resistive load of 80 k Ω (see Figure 5.10). For curved L-shape harvester 2, the maximum power output was 329 μ W at the optimal resistive load of 100 k Ω (see Figure 5.10). For curved L-shape harvester 3, the maximum power output was 349 μ W at the optimal resistive load of 117 k Ω (see Figure 5.10). The optimal resistive load is attributed to the internal impedance of the power harvester. When the external impedance (applied resistive load) matches the internal impedance, the power harvester generates the highest power.

The average power of the three prototypes was 350 μ W. Since the volume of the prototypes were 0.242 cm³, the average power density of the curved L-shape mass power harvesters was 1446 μ W/cm³.

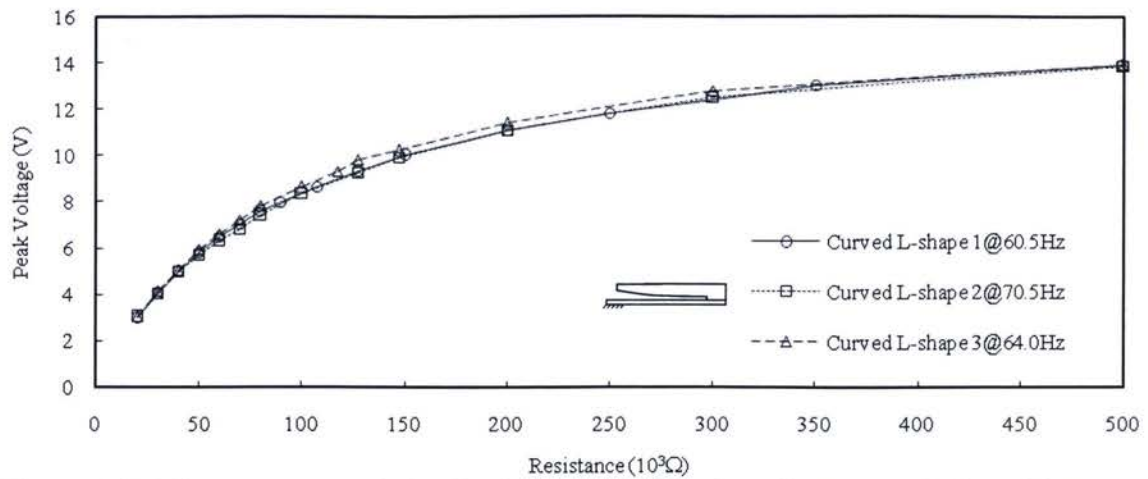


Figure 5.9 Voltage versus resistive loads for curved L-shape harvesters 1, 2, and 3 at an input acceleration of 0.75 g.

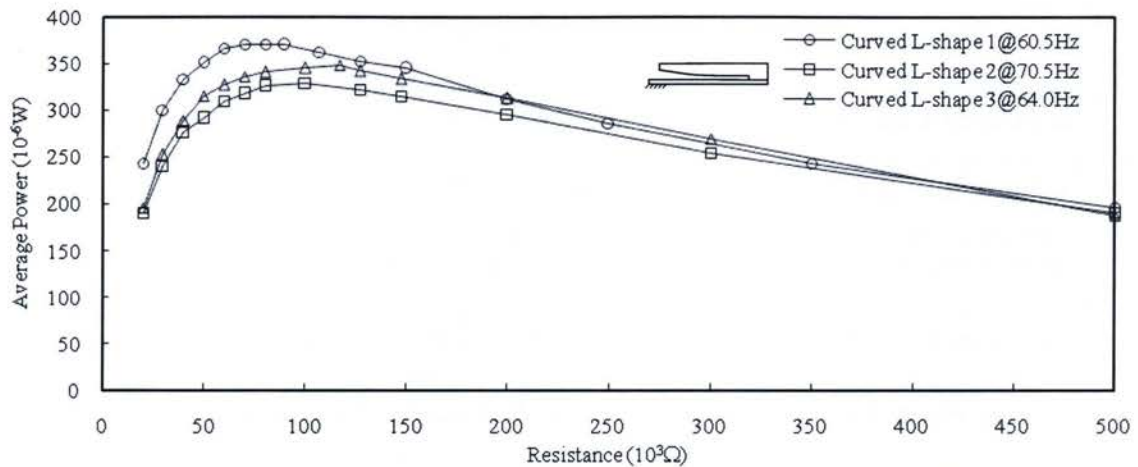


Figure 5.10 Power versus resistive loads for curved L-shape harvesters 1, 2, and 3 at an input acceleration of 0.75 g.

5.3 Shaker Results of the Block Shape Power Harvester

5.3.1 Fundamental Frequency of Block Shape Mass Harvester

The fundamental frequency of the block shape mass harvester was determined by measuring the open-circuit voltage output of the harvester from 10 to 120 Hz. An open-circuit voltage measurement of block shape harvester for 87 Hz @ 0.75 g is shown in Figure 5.11 and the signal was AC voltage of approximately ± 11.5 V.

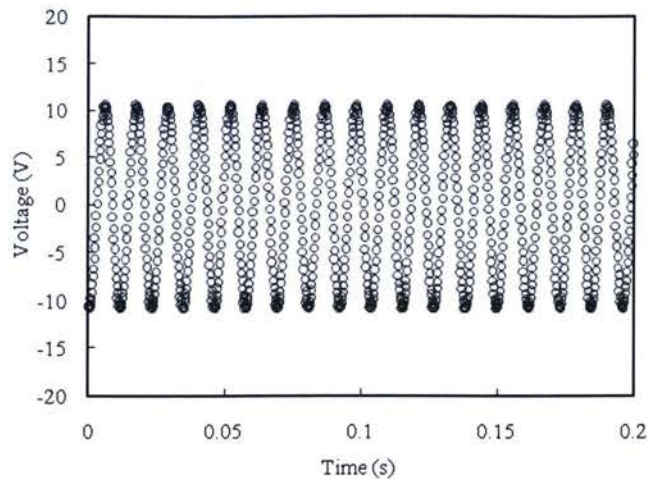


Figure 5.11 Open-circuit voltage output of block shape harvester at 87 Hz @ 0.75 g.

The peak open-circuit voltage output of block shape harvester from 80 Hz to 100 Hz at 0.25g, 0.50 g and 0.75 g are shown in Figure 5.12. When the input frequency approached the fundamental resonant frequency, the voltage increased significantly, the voltage then peaked at resonance and gradually decreased as input frequency moved away from the resonant frequency. For example, at 0.75 g in Figure 5.12, the voltage increased from 6.8 V @ 85.5 Hz to 10.3 V @ 86.0 Hz and to 11.8 V @ 86.5 Hz. The voltage reached a maximum of 11.8 V at the fundamental frequency of 87.0 Hz. Then the voltage dropped as the frequency increased and moved away from 87.0 Hz.

The measured fundamental frequency decreased with increasing input acceleration. As shown in Figure 5.12, the fundamental frequencies of block shape harvester were 90.0 Hz, 88.5 Hz, 87.0 Hz when the input accelerations were 0.25 g, 0.50 g and 0.75 g.

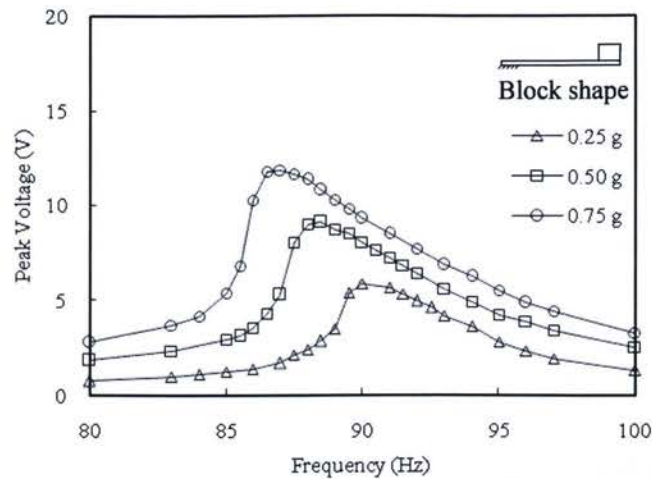


Figure 5.12 Peak open-circuit voltage versus frequency of block shape harvester at different input accelerations.

5.3.2 Power Output of Block Shape Mass Harvester

The power output of block shape mass harvester was determined by measuring the voltage output at different resistive loads for a frequency sweep of 10 to 120 Hz. An example of the voltage measurement, when block shape harvester was connected to 40 k Ω at an input of 86.5 Hz @ 0.75 g, is shown in Figure 5.13. The measured signal was AC voltage of approximately ± 4.4 V. The RMS value of the AC voltage was used to calculate the average power output of the block shape mass harvester.

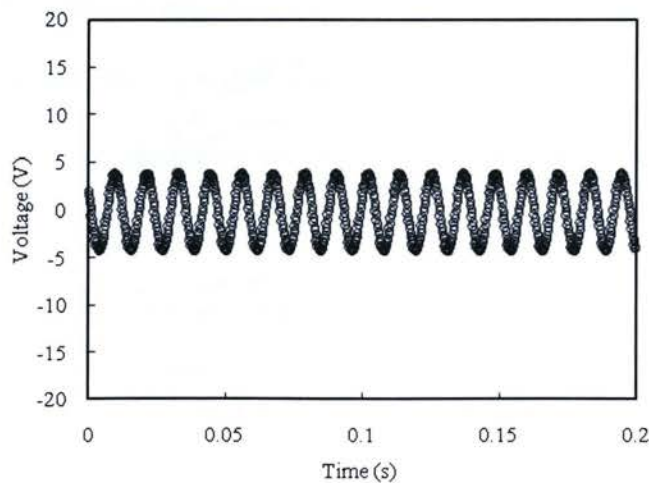


Figure 5.13 Voltage measurement of block shape harvester at 86.5 Hz @ 0.75 g for a resistive load of 40 k Ω .

The voltage versus frequency of block shape harvester for different resistive loads at a fixed input acceleration of 0.75 g is shown in Figure 5.14. The peak voltage increased with increasing resistive loads. The highest voltage of 10 k Ω , 40 k Ω , 150 k Ω , and 500 k Ω curves were measured to be 1.8 V, 4.4 V, 7.9 V and 10.4 V respectively (see Figure 5.14).

The resonant frequency of block shape harvester (input frequency that matches the natural frequency of the system) varied at different resistive loads. The resonant frequency at 10 k Ω , 40 k Ω , 150 k Ω and 500 k Ω curves were measured to be 83 Hz, 86.5 Hz, 88 Hz, and 87.5 Hz respectively (see Figure 5.14). The variation of resonant frequency with different resistive loads is attributed to the extra electrical damping induced on the power harvester system by the resistive loads.

The power versus frequency for block shape harvester at different resistive loads for a fixed input acceleration of 0.75 g is shown in Figure 5.15. The highest power output was measured at 40 k Ω for 86.5 Hz resonant frequency.

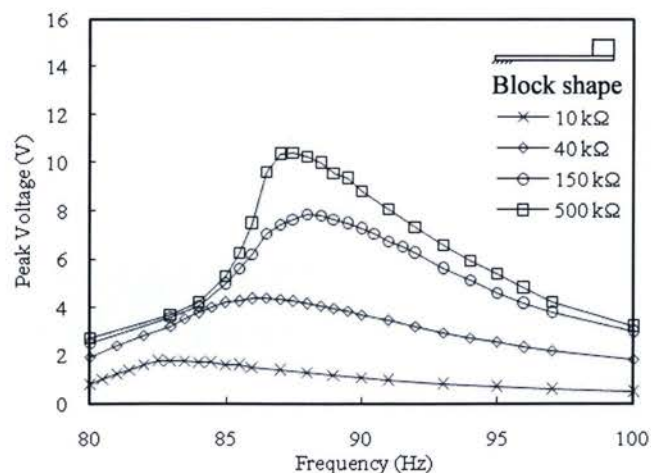


Figure 5.14 Voltage versus frequency of block shape harvester at different resistive loads for a fixed input of 0.75 g.

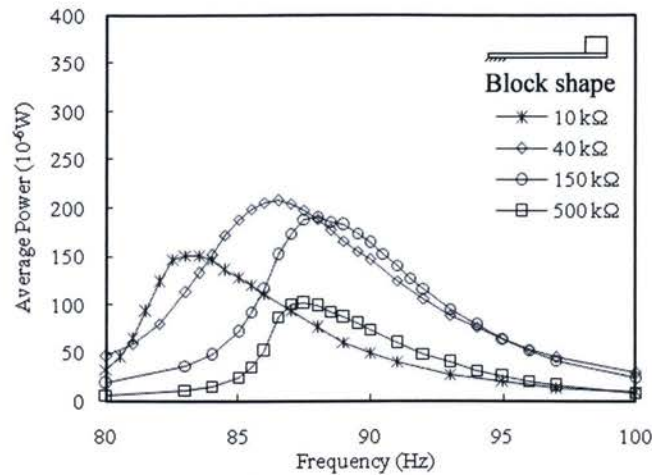


Figure 5.15 Power versus frequency of block shape harvester at different resistive loads for a fixed input of 0.75 g.

The voltage versus resistive load for block shape harvester at a fixed input of 86.5 Hz @ 0.75 g is shown in Figure 5.16. The voltage increased with increasing resistive load. The voltage increased from 1.4 V to 9.6 V when the resistive load increased from 10 kΩ to 500 kΩ.

The power output versus resistive load of block shape harvester is shown in Figure 5.17. The maximum power output was 208 μW at the optimal resistive load of 40 kΩ. The optimal resistive load is attributed to the internal impedance of the power harvester. When the external impedance (applied resistive load) matches the internal impedance, the power harvester generates the highest power.

Since the volume of the block shape mass harvester was 0.242 cm³, the power density was 859 μW/cm³.

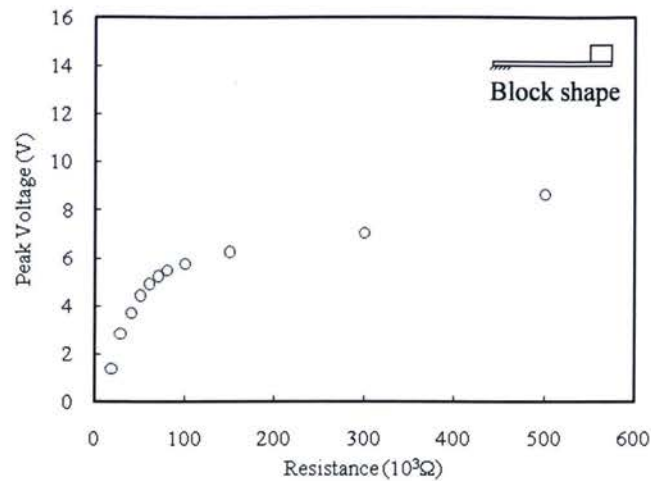


Figure 5.16 Voltage versus resistive loads for block shape harvester at a fixed input of 86.5Hz @ 0.75 g.

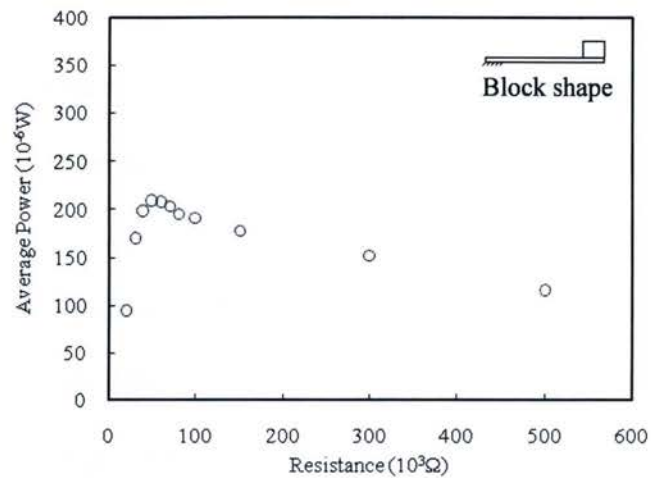


Figure 5.17 Power versus resistive loads for block shape harvester at a fixed input of 86.5Hz @ 0.75 g.

5.4 Comparison of Block Shape and Curved L-Shape Power Harvester's Shaker Results

For an input acceleration of 0.75 g, the average fundamental frequencies of the three curved L-shape mass harvesters were 60.0 Hz ~ 69.5 Hz and the fundamental frequency of the block shape mass harvester was 87.0 Hz. Thus, for the same power harvester volume, the curved L-shape mass harvester reduced the fundamental frequency by 20% ~ 31% compared to the block shape mass harvester.

The average power output of the three curved L-shape harvesters was 350 μW . The average power output of the block shape harvester was 208 μW . Thus, for the same volume of 0.242 cm^3 , the curved L-shape mass harvester increased the power density by 68% compared to the block shape mass harvester.

The discrepancy between the measured and designed fundamental frequencies (7% difference for curved L-shape harvester and 2% different for block shape harvester) and the variation in the performance of three curved L-shape mass harvesters can be attributed to manual assembly of the prototypes, which causes errors and variations in the free bending length l_{bend} (see Figure 1.5a and Figure 2.1a).

Chapter 6: Power Harvesting from Human Body's Motion

The curved L-shape mass power harvester 3 was attached to a shoe at the heel location to determine how much power can be generated from walking (see Figure 6.1 and Figure 6.2). The potential application of harvesting power from walking is health monitoring of the human body, i.e., measuring pulse rate, body temperature and blood pressure.

6.1 Setup of Treadmill Experiment

The athlete walking on the treadmill was 1.85 m tall and weighed 82 kg. A block diagram of the treadmill experiment setup is shown in Figure 6.3. The impact from walking provides periodic impact inputs to the power harvester. The output of the power harvester is decaying oscillating voltage for each impact input and the DAC was used to measure the output voltage.

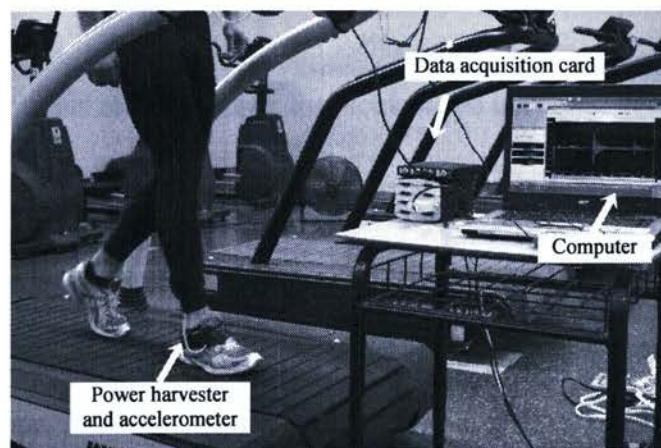


Figure 6.1 Setup of the walking experiment.

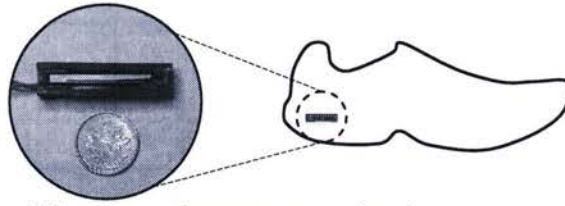


Figure 6.2 Attachment of the power harvester on the shoe.

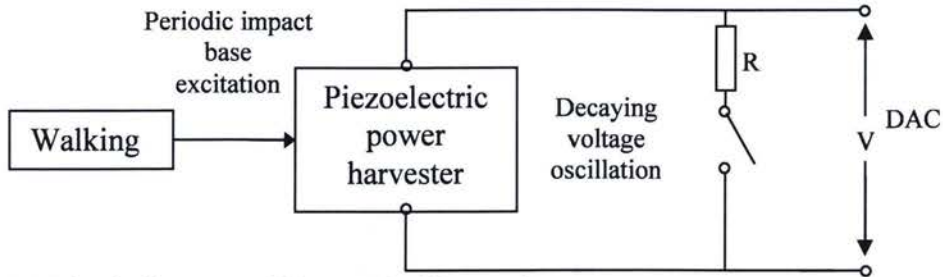


Figure 6.3 Block diagram of the treadmill experiment setup.

6.2 Measured Acceleration and Voltage Output of Curved L-Shape Harvester

As shown in Figure 6.4, the measured accelerations at the power harvester location for different walking speeds were periodic impacts. The measured impact acceleration increased as walking speed increased from 1.0 mph to 3.0 mph (see Figure 6.4). The highest measured acceleration was 15 g at a walking speed of 3.0 mph.

The output voltage of the power harvester was decaying oscillations for each impact acceleration input (see Figure 6.5). The output voltage of the power harvester increased with increasing walking speed. When the walking speed was higher (impact acceleration magnitude was high, see Figure 6.4), the magnitude and frequency of the output voltage was higher. The open-circuit RMS voltage of the power harvester at 1.0 mph to 3.0 mph walking speed is shown in Figure 6.6. The open-circuit RMS voltage increased from 0.85 V to 2.96 V when the walking speed increased from 1.0 mph to 3.0 mph.

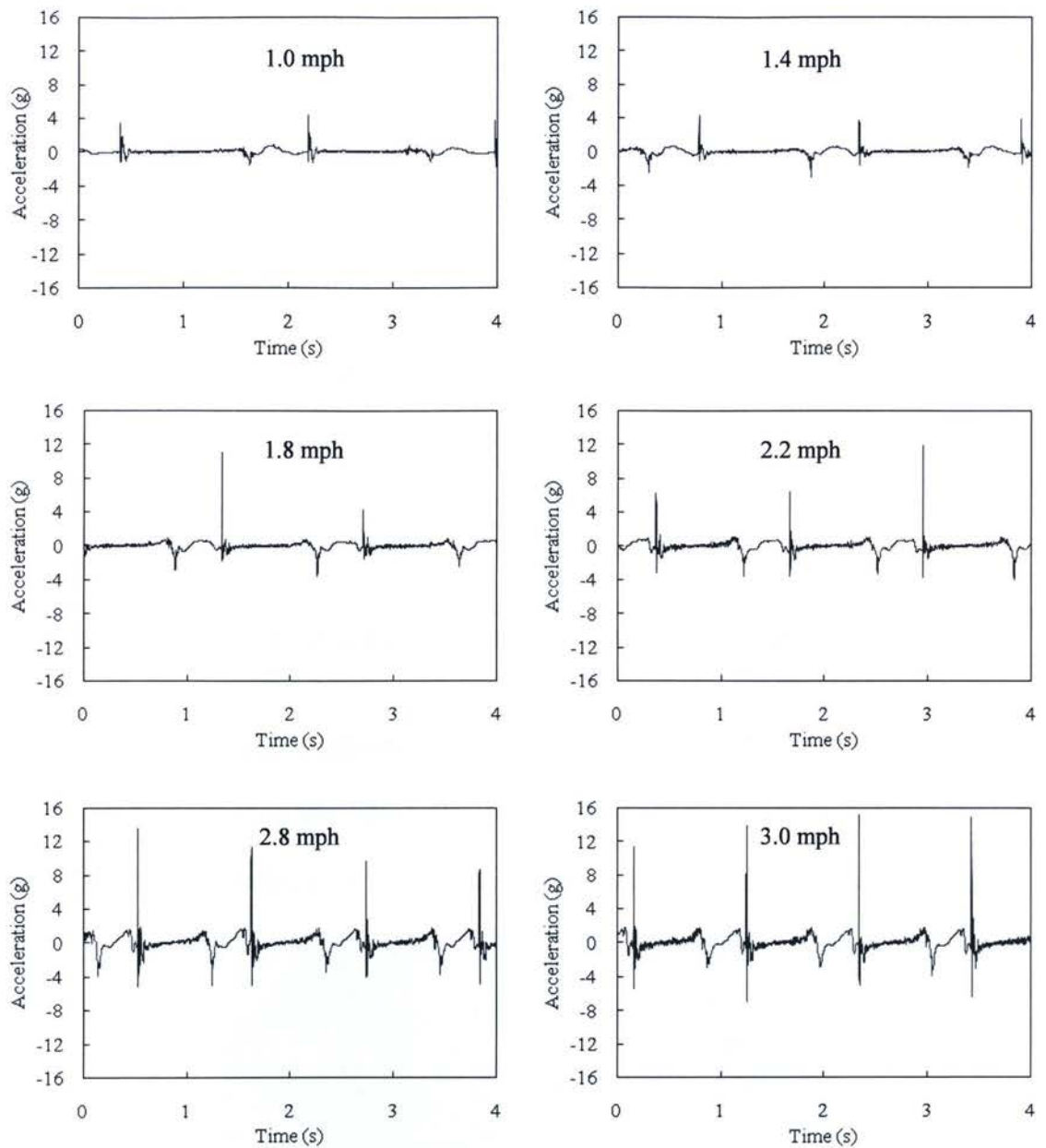


Figure 6.4 Measured acceleration versus time at different walking speeds.

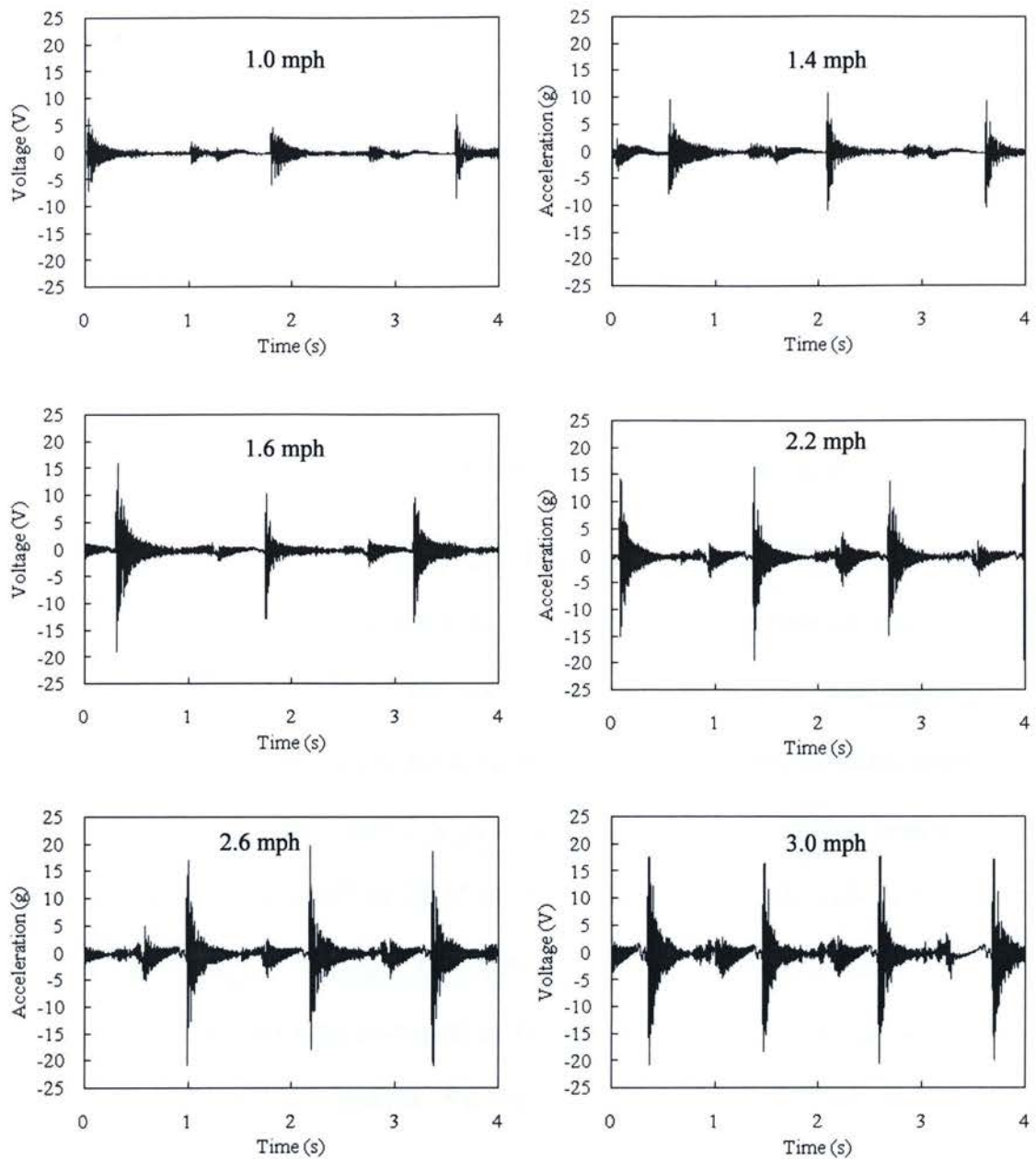


Figure 6.5 Output voltage of curved L-shape harvester versus time at different walking speeds.

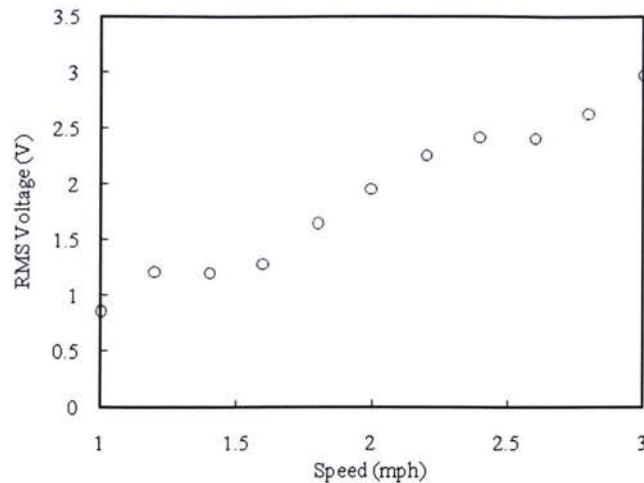


Figure 6.6 Open-circuit RMS voltage versus walking speed.

6.3 Power Output of Curved L-Shape Harvester

The power harvester was tested at different resistive loads and the measured voltages were used to determine the power output of the harvester. The RMS voltage versus resistive load at different walking speeds is shown Figure 6.7. The RMS voltage increased with increasing resistive load, e.g., at 3.0mph, the voltage increased from 1.0 V to 2.4 V when the resistor increased from 20 k Ω to 350 k Ω . The power versus resistive load at different walking speeds is shown in Figure 6.8. The power increased with increasing walking speed, e.g., the maximum power generated at 1.0 mph, 2.0 mph and 3.0 mph was 16.7 μ W, 29.2 μ W and 48.4 μ W respectively. The highest power generated by the power harvester was 48.4 μ W @ 40 k Ω at a walking speed of 3.0 mph.

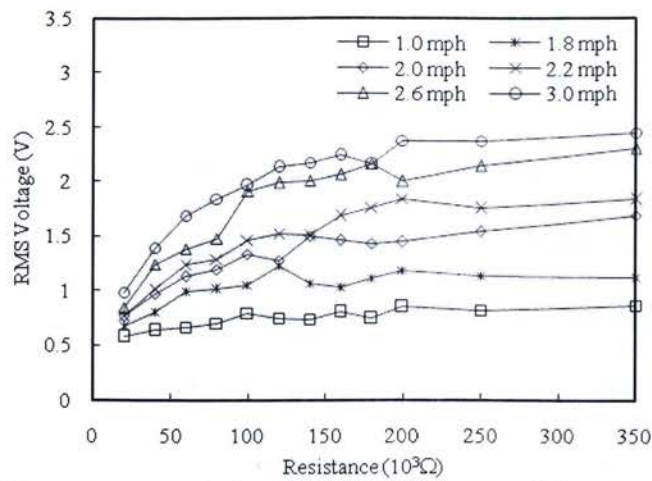


Figure 6.7 RMS voltage versus resistive load at different walking speeds.

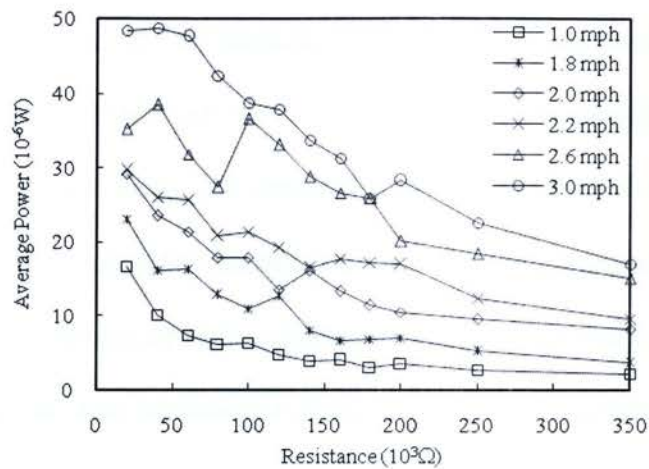


Figure 6.8 Power output versus resistive load at different walking speeds.

Chapter 7: Conclusions and Recommendations for Future Work

A cantilever piezoelectric power harvester with a curved L-shape mass was developed and tested under various conditions. Simulation and experimental results showed that the curved L-shape mass power harvester has a lower fundamental frequency and higher power density compared with the conventional block shape and U-shape mass harvesters.

The curve L-shape, block shape, and U-shape mass harvesters were designed and compared based on having the same overall volume and having the same fundamental frequency. For a volume of 0.242 cm^3 , the curved L-shape mass design has a fundamental frequency that was 24% and 15% lower than the block shape and U-shape mass designs respectively. For a fundamental frequency of 65 Hz, the curved L-shape mass design has a volume that was 69% and 25% smaller than the block shape and U-shape mass designs respectively, which leads to an increase of 69% and 25% in power density respectively.

Three curved L-shape mass harvesters and a block shape harvester were fabricated and tested on a shaker. At an input acceleration of 0.75 g, the curved L-shape mass harvester lowered the fundamental frequency by 20% ~ 31% and increased the power density by 68% compared to the conventional block shape mass harvester. The curved L-shape mass harvesters generated an average power of 350 μW with a power density of 1446 $\mu\text{W}/\text{cm}^3$.

An application of power harvesting from human body's motion using the curved L-shape mass power harvester was demonstrated. The power harvester was attached to a

shoe of a person walking at 1.0 mph to 3.0 mph on a treadmill. At a walking speed of 3.0 mph, the curved L-shape mass power harvester generated 48.4 μ W.

The future work of this project should focus on the following:

- 1) Reliability of the curved L-shape mass harvester prototype: It was observed during the treadmill test that when the harvester is subjected to high input accelerations (during jogging speed from 5 mph to 10 mph), the power harvester has difficulty surviving. The industrial strength epoxy that bonds the proof mass and beam can fail, which results in the mass getting off the beam or the beam getting off the base. The piezoelectric beam itself could fail due to the high stresses in the beam. A new and better method should be developed to strengthen the bonding of components and to better protect the piezoelectric beam in high acceleration conditions. A potential solution to strengthen bonding is wrapping the components using a thin (yet strong) wire and sealing the wire with epoxy. A potential solution to better protecting the piezoelectric beam is to use softer (rubber type) stoppers.
- 2) Development of curved L-shaped mass harvester based on applications: For example, real-time pressure monitoring inside car tires and health monitoring of human body during walking/jogging/running has abundant vibration energy. A curved L-shape mass harvester that is even smaller can be designed and fabricated to harvest the abundant power to extend battery life or eliminate the need for batteries.

Publications

W. Li, S. He, and S. D. Yu, "A Novel Design of a Piezoelectric Micro Power Generator," *in Proceedings of the Canadian Society of Mechanical Engineers 2008 Forum*, June 5 – 8, Ottawa, Canada.

W. G. Li, S. He, and S.D. Yu, "Improving Power Density of a Cantilever Piezoelectric Power Harvester through a Curved L-Shape Proof Mass," *IEEE Trans. on Industrial Electronics*, in press.

References

- [1] S. Roundy, P. K. Wright, and J. Rabaey, "A study of low level vibrations as a power source for wireless sensor nodes," *Computer Communications*, vol. 26, no. 11, pp. 1131-1144, 2003.
- [2] Bosch Sensortec (2009). <http://www.bosch-sensortec.com>. Accessed April 2009.
- [3] Jlh Labs (2004). <http://www.jlhlab.com>. Accessed April 2009.
- [4] St. Jude Medical (2009). <http://www.sjm.com>. Accessed April 2009.
- [5] Environment Canada (2007). 'Canadian Consumer Battery Baseline Study – Final Report'. <http://www.ec.gc.ca/nopp/docs/rpt/battery/en/toc.cfm?>. Accessed April 2009.
- [6] C. B. Williams, and R. B. Yates, "Analysis of a micro-electric generator for microsystems," *Sensors and Actuators A: Physical*, vol. 52, pp. 8-11, 1996.
- [7] R. Amirtharajah, and A. P. Chandrakasan, "Self-powered signal processing using vibration-based power generation," *Solid-State Circuits, IEEE Journal of*, vol. 33, no. 5, pp. 687-695, 1998.
- [8] P. Glynne-Jones, M. J. Tudor, S. P. Beeby *et al.*, "An electromagnetic, vibration-powered generator for intelligent sensor systems," *Sensors and Actuators, A: Physical*, vol. 110, no. 1-3, pp. 344-349, 2004.
- [9] D. Spreemann, Y. Manoli, B. Folkmer *et al.*, "Non-resonant vibration conversion," *Journal of Micromechanics and Microengineering*, vol. 16, no. 9, pp. S169-S173, 2006.
- [10] B. H. Stark, and T. C. Green, "Comparison of SOI power device structures in power converters for high-voltage, low-charge electrostatic microgenerators," *IEEE Transactions on Electron Devices*, vol. 52, no. 7, pp. 1640-1648, 2005.
- [11] S. Meninger, J. O. Mur-Miranda, R. Amirtharajah *et al.*, "Vibration-to-electric energy conversion," *IEEE Transactions on Very Large Scale Integration (VLSI) Systems*, vol. 9, no. 1, pp. 64-76, 2001.
- [12] P. Miao, P. D. Mitcheson, A. S. Holmes *et al.*, "Mems inertial power generators for biomedical applications," *Microsystem Technologies*, vol. 12, no. 10-11, pp. 1079-1083, 2006.
- [13] H. A. Sodano, D. J. Inman, and G. Park, "Comparison of piezoelectric energy harvesting devices for recharging batteries," *Journal of Intelligent Material Systems and Structures*, vol. 16, no. 10, pp. 799-807, 2005.

- [14] S. Roundy, and P. K. Wright, "A piezoelectric vibration based generator for wireless electronics," *Smart Materials and Structures*, vol. 13, no. 5, pp. 1131-1142, 2004.
- [15] S. Roundy, P. Wright, and J. Rabaey, *Energy Scavenging for Wireless Sensor Networks with Special Focus on Vibrations*: Springer, 2003.
- [16] S. J. Roundy, "Energy Scavenging for Wireless Sensor Nodes with a Focus on Vibration to Electricity Conversion ", Ph.D. dissertation, Dept. Mech. Eng., U.C. Berkley., Berkley, CA., 2003.
- [17] C. S. Lee, J. Joo, S. Han *et al.*, "Multifunctional transducer using poly (vinylidene fluoride) active layer and highly conducting poly (3,4-ethylenedioxythiophene) electrode: Actuator and generator," *Applied Physics Letters*, vol. 85, no. 10, pp. 1841-1843, 2004.
- [18] C. S. Lee, J. Joo, S. Han *et al.*, "Poly (vinylidene fluoride) transducers with highly conducting poly (3,4-ethylenedioxythiophene) electrodes," *Synthetic Metals*, vol. 152, no. 1-3, pp. 49-52, 2005.
- [19] L. M. Swallow, J. K. Luo, E. Siores *et al.*, "A piezoelectric fibre composite based energy harvesting device for potential wearable applications," *Smart Materials and Structures*, vol. 17, no. 2, 2008.
- [20] D. L. Churchill, M. J. Hamel, C. P. Townsend *et al.*, "Strain Energy Harvesting for Wireless Sensor Networks," *Proceedings of SPIE - The International Society for Optical Engineering*, vol. 5055, pp. 319-327, 2003.
- [21] F. Mohammadi, A. Khan, and R. B. Cass, "Power generation from piezoelectric lead zirconate titanate fiber composites," *Proc. Materials Research Symp.* vol. 736, pp. 263-268, 2002.
- [22] H. A. Sodano, J. Lloyd, and D. J. Inman, "An experimental comparison between several active composite actuators for power generation," *Proceedings of SPIE - The International Society for Optical Engineering*, vol. 5390, pp. 370-378, 2004.
- [23] J. Baker, S. Roundy, and P. Wright, "Alternative geometries for increasing power density in vibration energy scavenging for wireless sensor networks," *Collection of Technical Papers - 3rd International Energy Conversion Engineering Conference*, vol. 2, pp. 959-970, 2005.
- [24] S. Roundy, E. S. Leland, J. Baker *et al.*, "Improving power output for vibration-based energy scavengers," *IEEE Pervasive Computing*, vol. 4, no. 1, pp. 28-36, 2005.
- [25] L. Mateu, and F. Moll, "Optimum Piezoelectric Bending Beam Structures for Energy Harvesting using Shoe Inserts," *Journal of Intelligent Material Systems and Structures*, vol. 16, no. 10, pp. 835-845, 2005.

- [26] Y. B. Jeon, R. Sood, J. H. Jeong *et al.*, "MEMS power generator with transverse mode thin film PZT," *Sensors and Actuators, A: Physical*, vol. 122, no. 1 SPEC. ISS., pp. 16-22, 2005.
- [27] T. H. Ng, and W. H. Liao, "Sensitivity analysis and energy harvesting for a self-powered piezoelectric sensor," *Journal of Intelligent Material Systems and Structures*, vol. 16, no. 10, pp. 785-797, 2005.
- [28] Zheng, and Y. Xu, "Asymmetric air-spaced cantilevers for vibration energy harvesting," *Smart Materials and Structures*, vol. 17, no. 5, pp. 055009, 2008.
- [29] S. Priya, "Modeling of electric energy harvesting using piezoelectric windmill," *Applied Physics Letters*, vol. 87, no. 18, pp. 1-3, 2005.
- [30] S. Priya, C. T. Chen, D. Fye *et al.*, "Piezoelectric Windmill: A novel solution to remote sensing," *Japanese Journal of Applied Physics, Part 2: Letters*, vol. 44, no. 1-7, pp. L104-L107, 2005.
- [31] S. Priya, "Modeling of electric energy harvesting using piezoelectric windmill," *Applied Physics Letters*, vol. 87, no. 18, pp. 1-3, 2005.
- [32] C. T. Chen, R. A. Islam, and S. Priya, "Electric energy generator," *IEEE Transactions on Ultrasonics, Ferroelectrics, and Frequency Control*, vol. 53, no. 3, pp. 656-661, 2006.
- [33] R. Myers, M. Vickers, H. Kim *et al.*, "Small scale windmill," *Applied Physics Letters*, vol. 90, no. 5, 2007.
- [34] S. Priya, "Advances in energy harvesting using low profile piezoelectric transducers," *Journal of Electroceramics*, vol. 19, no. 1, pp. 165-182, 2007.
- [35] H. W. Kim, A. Batra, S. Priya *et al.*, "Energy harvesting using a piezoelectric "cymbal" transducer in dynamic environment," *Japanese Journal of Applied Physics, Part 1: Regular Papers and Short Notes and Review Papers*, vol. 43, no. 9 A, pp. 6178-6183, 2004.
- [36] H. W. Kim, S. Priya, K. Uchino *et al.*, "Piezoelectric energy harvesting under high pre-stressed cyclic vibrations," *Journal of Electroceramics*, vol. 15, no. 1, pp. 27-34, 2005.
- [37] H. Kim, S. Priya, H. Stephanou *et al.*, "Consideration of impedance matching techniques for efficient piezoelectric energy harvesting," *IEEE Transactions on Ultrasonics, Ferroelectrics, and Frequency Control*, vol. 54, no. 9, pp. 1851-1858, 2007.
- [38] J. Yang, H. Zhou, Y. Hu, and Q. Jiang, "Performance of a piezoelectric harvester in thickness-stretch mode of a plate," *IEEE Trans. Ultrason. Ferroelectr. Freq. Control*, vol 52, pp. 1872-6, 2005.

- [39] C. D. Richards, M. J. Anderson, D. F. Bahr, and R. F. Richards, "Efficiency of energy conversion for devices containing a piezoelectric component," *J. Micromech. Microeng.*, vol. 14, pp. 717–21, 2004.
- [40] J. Cho, M. Anderson, R. Richards, D. Bahr and C. Richards, "Optimization of electromechanical coupling for a thin-film PZT membrane: I. modeling," *J. Micromech. Microeng.*, vol. 15, pp. 1797–803, 2005.
- [41] J. Cho, M. Anderson, R. Richards, D. Bahr and C. Richards, "Optimization of electromechanical coupling for a thin-film PZT membrane: II. Experiment," *J. Micromech. Microeng.*, vol. 15, pp. 1804–9, 2005.
- [42] S. R. Platt, S. Farritor, and H. Haider, "The use of piezoelectric ceramics for electric power generation within orthopedic implants," *IEEE Trans. Mechatronics*, vol. 10, pp. 455–61, 2005.
- [43] N.S. Shenck and J. A. Paradiso, "Energy scavenging with shoe-mounted piezoelectrics," *IEEE Micro*, vol. 21, pp. 30–42, 2001.
- [44] H. A. Sodano, D. J. Inman, and G. Park, "A review of power harvesting from vibration using piezoelectric materials," *Shock and Vibration Digest*, vol. 36, no. 3, pp. 197–205, 2004.
- [45] S. R. Anton, and H. A. Sodano, "A review of power harvesting using piezoelectric materials (2003–2006)," *Smart Materials and Structures*, vol. 16, no. 3, pp. R1–R21, 2007.
- [46] K. A. Cook-Chennault, N. Thambi, and A. M. Sastry, "Powering MEMS portable devices - a review of non-regenerative and regenerative power supply systems with special emphasis on piezoelectric energy harvesting systems," *Smart Materials and Structures*, vol. 17, no. 4, pp. 043001, 2008.
- [47] A. Khaligh, P. Zheng, and C. Zheng, "Kinetic Energy Harvesting using Piezoelectric and Electromagnetic Technologies-State of the Art," *IEEE Trans. on Industrial Electronics*, vol. 56, pp. 1–1, 2009.
- [48] G. K. Ottman, H. F. Hofmann, and G. A. Lesieutre, "Optimized piezoelectric energy harvesting circuit using step-down converter in discontinuous conduction mode," *IEEE Transactions on Power Electronics*, vol. 18, no. 2, pp. 696–703, 2003.
- [49] T. T. Le, J. Han, A. Von Jouanne *et al.*, "Piezoelectric micro-power generation interface circuits," *IEEE Journal of Solid-State Circuits*, vol. 41, no. 6, pp. 1411–1419, 2006.
- [50] M. A. Adeeb, H. Nguyen, S. K. Islam *et al.*, "A low-power RF integrated circuit for implantable sensors," *Analog Integrated Circuits and Signal Processing*, vol. 47, no. 3, pp. 355–363, 2006.

- [51] E. Lefeuvre, A. Badel, C. Richard *et al.*, "Energy harvesting using piezoelectric materials: Case of random vibrations," *Journal of Electroceramics*, vol. 19, no. 4, pp. 349-355, 2007.
- [52] A. Badel, D. Guyomar, E. Lefeuvre *et al.*, "Piezoelectric energy harvesting using a synchronized switch technique," *Journal of Intelligent Material Systems and Structures*, vol. 17, no. 8-9, pp. 831-839, 2006.
- [53] D. Guyomar, A. Badel, E. Lefeuvre *et al.*, "Toward energy harvesting using active materials and conversion improvement by nonlinear processing," *IEEE Transactions on Ultrasonics, Ferroelectrics, and Frequency Control*, vol. 52, no. 4, pp. 584-594, 2005.
- [54] M. Lallart, L. Garbuio, L. Petit *et al.*, "Double synchronized switch harvesting (DSSH): A new energy harvesting scheme for efficient energy extraction," *IEEE Transactions on Ultrasonics, Ferroelectrics, and Frequency Control*, vol. 55, no. 10, pp. 2119-2130, 2008.
- [55] E. Lefeuvre, A. Badel, C. Richard *et al.*, "High performance piezoelectric vibration energy reclamation." pp. 379-387.
- [56] E. Lefeuvre, G. Sebald, D. Guyomar *et al.*, "Materials, structures and power interfaces for efficient piezoelectric energy harvesting," *Journal of Electroceramics*, vol. 22, no. 1-3, pp. 171-179, 2009.
- [57] D. J. Inman. *Engineering Vibrations, 2nd Edition*: Prentice Hall, 2000.
- [58] Ansys 11.0, A Finite Element Analysis Package, Ansys, Inc., Canonsburg, PA, 2003.
- [59] Piezo Systems Inc. (2009). <http://www.piezo.com>. Accessed April 2009.